International Journal of Greenhouse Gas Control 27 (2014) 120–138

Contents lists available at ScienceDirect

International Journal of Greenhouse Gas Control

journal homepage: www.elsevier.com/locate/ijggc

Geoelectrical baseline model of the subsurface of the Hontomín site (Spain) for CO_2 geological storage in a deep saline aquifer: A 3D magnetotelluric characterisation

Xènia Ogaya[a,*], Pilar Queralt[a], Juanjo Ledo[a], Álex Marcuello[a], Alan G. Jones[b]

[a] Departament de Geodinàmica i Geofísica, Facultat de Geologia, GEOMODELS Research Institute, Universitat de Barcelona, C/ Martí i Franquès s/n, 08028 Barcelona, Spain
[b] Dublin Institute for Advanced Studies, School of Cosmic Physics, Dublin 2, Ireland

ARTICLE INFO

Article history:
Received 18 January 2014
Received in revised form 26 March 2014
Accepted 29 April 2014

Keywords:
CO_2 storage
Geoelectrical baseline model
Geophysical imaging
3D modelling
Magnetotellurics
Electrical resistivity

ABSTRACT

The magnetotelluric (MT) method was used to characterise the underground research laboratory (URL) for CO_2 storage in a deep saline aquifer at Hontomín (Spain). A total grid of 109 closely-spaced broadband MT sites was acquired in the study area covering an areal extent of 3×5 km^2. Different three-dimensional (3D) inversion codes were employed to invert the MT data in the period range of 0.001–10 s (frequency range 1000–0.1 Hz), with all of them giving similar results. The final preferred 3D model validates a previously published two-dimensional (2D) MT study and is supported by a variety of multidisciplinary data (e.g., well log, 3D seismic and hydrogeochemistry data). The 3D model constitutes the baseline electrical resistivity model of the site that will be used for the future time-lapse electromagnetic (EM) monitoring experiments of the URL. The 3D resistivity distribution shows the dome-like structure of the saline aquifer and images fracture regions, thus identifying the most likely leakage pathways and consequently, the monitoring requirements of the Hontomín site.

1. Introduction

Monitoring of CO_2 storage sites permits control of gas injection and storage operations, detection of possible leakage, and support of the required safety conditions (IPCC, 2005; NETL, 2009). Different geophysical techniques are presented as suitable for monitoring purposes and a number of multidisciplinary monitoring schemes have been designed to study and control the evolution of the injected CO_2 plume (Hoversten and Gasperikova, 2005; IPCC, 2005; Giese et al., 2009; NETL, 2009; JafarGandomi and Curtis, 2011; Sato et al., 2011). Electric and electromagnetic (EM) methods have been demonstrated to be valuable as they constrain the electrical conductivity of the storage complex and offer a high degree of complementarity between their different techniques to study the different scales and depths of interest in a storage site (Kiessling et al., 2010; Streich et al., 2010; Girard et al., 2011; Bergmann et al., 2012; Vilamajó et al., 2013). The electrical conductivity of the Earth materials (also commonly defined in terms of its inverse, electrical resistivity) is essentially a transport property of the medium, compared to the propagation velocity of elastic waves which is a property that is associated to the transmission of mechanical energy. It has a far wider range of variation than seismic velocity or rock density (Bedrosian, 2007) and is more sensitive to CO_2 saturation compared to other techniques (Lumley, 2010; MacGregor, 2012). Electrical conductivity is a physical property sensitive to the nature of the rock constituents (mineralogy composition of the rock) but also to the characteristics of the pore space; it depends on fluid salinity, temperature, porosity, pore connectivity, saturation and pressure (Bedrosian, 2007). Archie's law (Archie, 1942) describes reasonably well the bulk electrical conductivity of the rock as a function of these parameters. In the context of CO_2 monitoring, the estimation of some of these parameters is critical to locate the gas plume and understand CO_2 migration (Bourgeois and Girard, 2010; Nakatsuka et al., 2010; Alemu et al., 2011; MacGregor, 2012; Börner et al., 2013).

For most techniques, the changes produced by the injection of the CO_2 are identified and quantified carrying out a comparative analysis with the reference pre-injection state (monitoring based on repeated time-lapse studies). For that reason, a thorough characterisation must be taken first to define a high-resolution baseline

* Corresponding author at: Facultat de Geologia, Dept. Geodinàmica i Geofísica, C/Martí i Franquès s/n, 08028 Barcelona, Spain. Tel.: +34 934034028; fax: +34 934021340.
E-mail addresses: xeniaogaya@ub.edu, xeniaogaya@gmail.com (X. Ogaya).

http://dx.doi.org/10.1016/j.ijggc.2014.04.030
1750-5836/

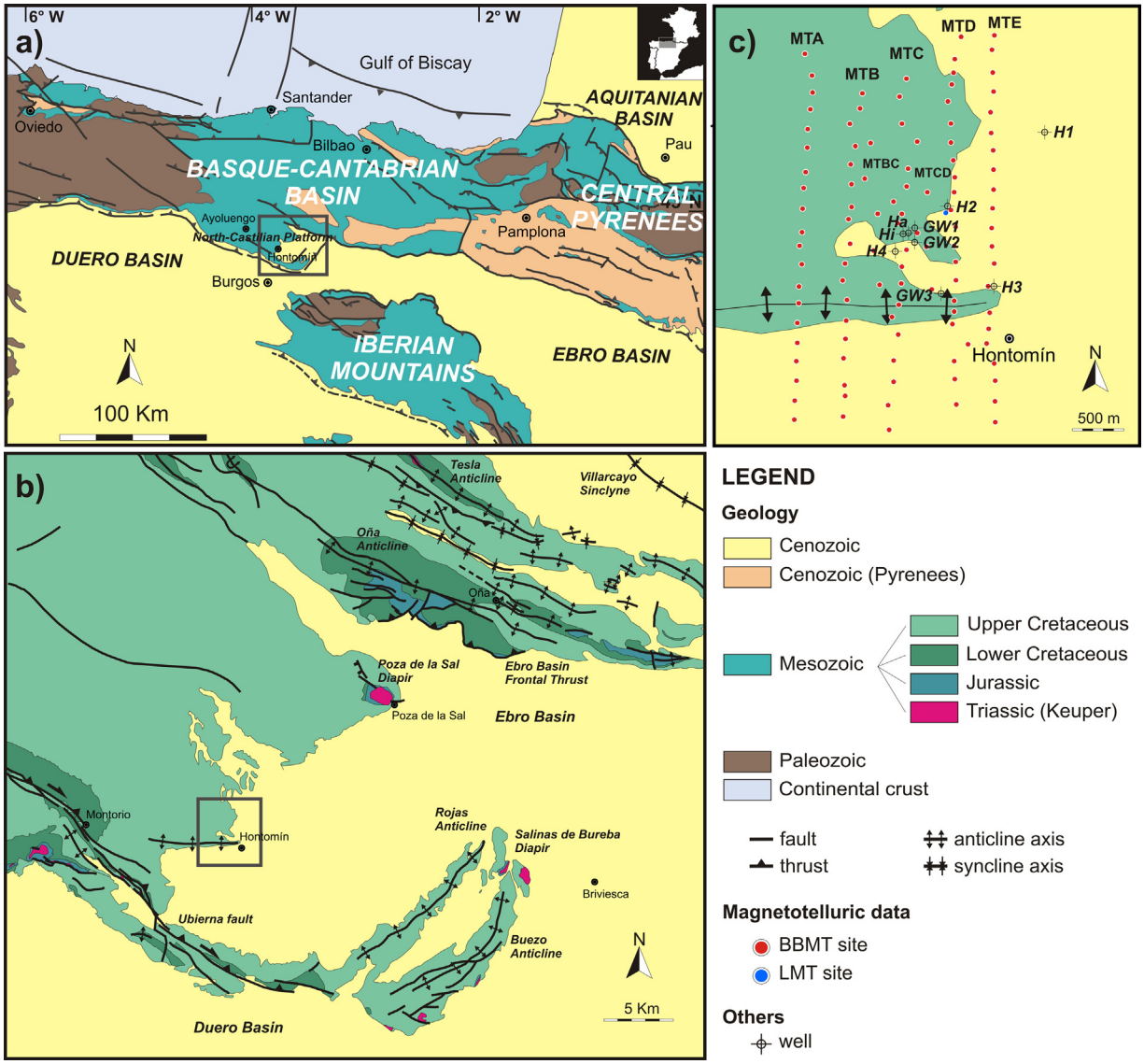

Fig. 1. Geological maps of the study area: (a) geological map of the Basque-Cantabrian Basin indicating the North-Castilian Platform and the location of the study area (modified from Muñoz, 2002); (b) geological map of the Hontomín surrounding area indicating the location of the Hontomín structure; (c) red and blue dots show the location of the broadband MT (BBMT) and long period MT (LMT) sites, respectively. Also indicated are the acronyms of the various profiles (MTA-MTE) and the locations of the wells H1–H4, GW1–GW3 and Hi-Ha. (For interpretation of the references to colour in this figure legend, the reader is referred to the web version of this article.)

model of the storage site subsurface. In the underground research laboratory (URL) for CO_2 storage in a deep saline aquifer of Hontomín (Spain; described below), a large number of multidisciplinary experiments are being undertaken to characterise the subsurface in order to be able to monitor the expected CO_2 plume evolution (e.g., Rubio et al., 2011; Buil et al., 2012; Benjumea et al., 2012; Ogaya et al., 2012; Alcalde et al., 2013a,b; Canal et al., 2013; Elío et al., 2013; Nisi et al., 2013; Ogaya et al., 2013; Quintà, 2013; Ugalde et al., 2013; Vilamajó et al., 2013). Since the applicability and sensitivity of monitoring techniques depends on the site characteristics, diverse EM techniques are being assessed for different purposes according to their resolution and penetration depth.

The magnetotelluric (MT) method has demonstrated its validity to characterise the subsurface of the Hontomín site providing the first two-dimensional (2D) geoelectrical model of the URL (Ogaya et al., 2013). Controlled-source EM (CSEM) techniques have indicated their feasibility to monitor the Hontomín site and detect small volumes of CO_2 (Vilamajó et al., 2013). Moreover, the EM noise of the study area has been analysed and characterised (Escalas et al., 2013) in order to design strategies to deal with it.

This work addresses the extension of the MT characterisation presented in Ogaya et al. (2013). In general, the MT method has been used in both regional (e.g., Rosell et al., 2011) and local (e.g., Ogaya et al., 2013) characterisation work since it is the only EM technique with a penetration depth ranging from tens of metres to hundreds of kilometres. Moreover, its tensorial character enables determination of the dominant directionality of geological structures and subsurface processes, and their variation with depth. In the past years, thanks to the progress made in 3D MT inversion algorithms (Avdeev, 2005; Siripunvaraporn, 2012), a number of MT studies have been undertaken in 3D in order to overcome the limitations of 2D interpretation (Ledo et al., 2002). Some of these investigations were focussed on near surface structures demonstrating the suitability of the method in a variety of contexts: mineral exploration (Tuncer et al., 2006; Farquharson and Craven, 2009; Xiao et al., 2010); waste site characterisation (Newman et al., 2003); volcano and geothermal studies (Heise et al., 2008; Newman et al., 2008; Ingham et al., 2009; Ghaedrahmati et al., 2013) and hydrocarbon exploration (He et al., 2010; Zhdanov et al., 2011). In CO_2 geological storage contexts,

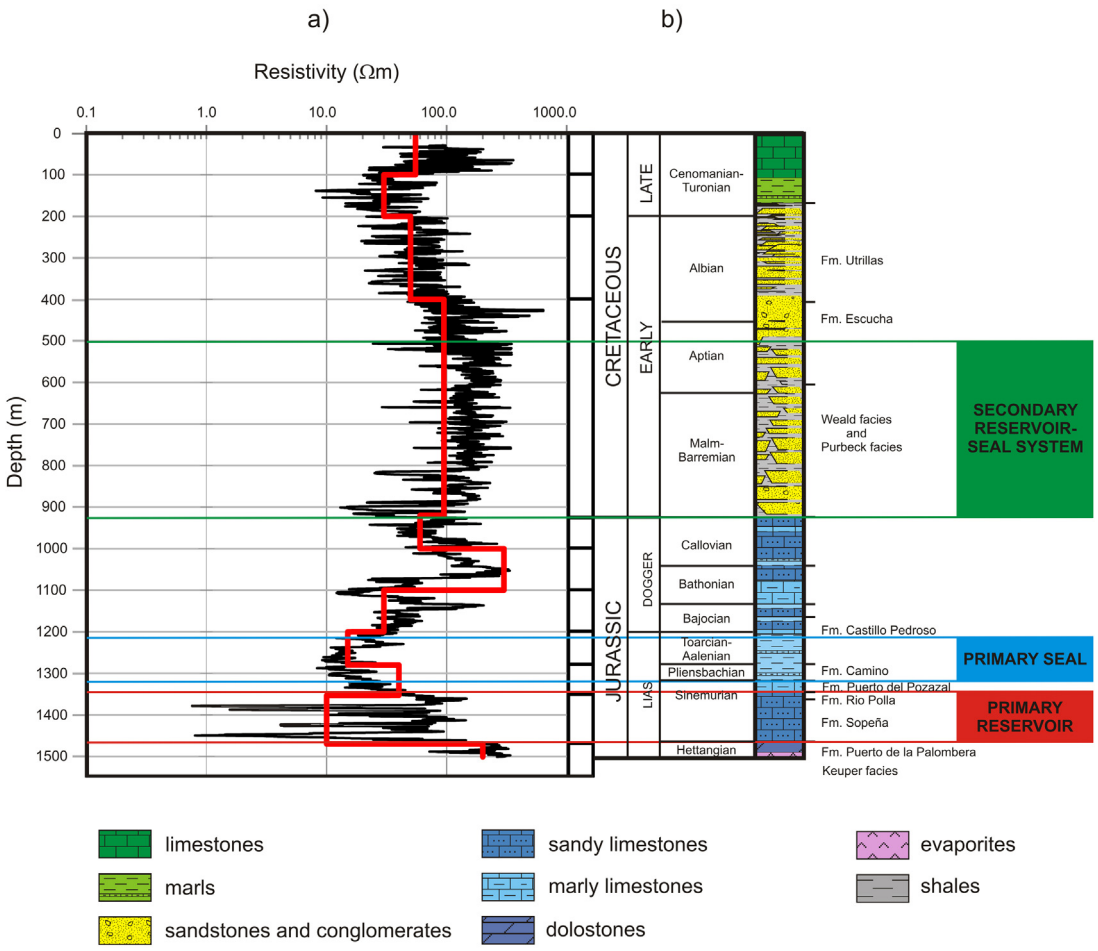

Fig. 2. Electrical resistivity of the different facies and formations: (a) in black, H2 resistivity log data and in red, H2 one-dimensional resistivity model (Ogaya et al., 2013); (b) stratigraphic column of the Hontomín site at H2 well showing Triassic to Cretaceous materials. Primary and secondary reservoir-seal systems are indicated. Depths are given in terms of true vertical depth (TVD).

this work constitutes the first 3D MT characterisation survey of an URL.

In agreement with the results of the dimensionality analysis presented in Ogaya et al. (2012), 3D inversion and forward modelling of the complete MT data set was undertaken, combining the inverse code described by Mackie and Madden (1993) subsequently developed and implemented by Geosystem, and the ModEM inverse code presented by Egbert and Kelbert (2012). The process was also corroborated using the WSINV3DMT inverse code (Siripunvaraporn et al., 2005). The final 3D model defines the geoelectrical baseline model of the Hontomín URL subsurface that will establish the point of comparison for subsequent EM monitoring surveys of the site.

2. The Hontomín site

The Hontomín URL is a Technological Development Plant (TDP) for CO_2 storage in a deep saline aquifer; the project is led by the Fundación Ciudad de la Energía – CIUDEN. The Hontomín site is a non-commercial project and the injection is limited to 100 kilotons by regulation. However, no more than 20 kilotons are planned to be injected which corresponds to an approximate volume of $135 \times 135 \times 25\ m^3$ at 1500 m TVD (true vertical depth). The volume was estimated according to the variation of CO_2 density with depth, for hydrostatic pressure and a geothermal gradient of 25 °C/km from 15° at the surface (Fig. 5.2 in IPCC, 2005)

The URL is located in the southern sector of the Basque-Cantabrian Basin (Western Pyrenees, Spain; Fig. 1). The boundaries of the Hontomín structure are the Ubierna Fault to the south (Tavani et al., 2011), the Ebro basin to the east and the Duero basin to the west (Fig. 1). The geological setting of the study area pertinent to EM studies was described in detail in Ogaya et al. (2013) and will be summarised below.

Former hydrocarbon exploration activity in the region provided 2D seismic profiles and well-log data (H1, H2, H3 and H4; Fig. 1c). These geological and geophysical data, as well as recent studies including 3D reflection seismics (Alcalde et al., 2013a,b), gravimetry (Rubio et al., 2011) and magnetotellurics (Ogaya et al., 2013), indicate that the Hontomín site is a smooth Jurassic domed anticline structure cored by Upper Triassic evaporites (Keuper facies; Quintà, 2013; Fig. 2). The overall lateral extent of the structure is $3 \times 5\ km^2$.

Two wells are planned in the URL (Fig. 1c): the injection well (Hi) and the monitoring well (Ha). They will be placed on the crest of the Jurassic dome according to the geological interpretation derived from the available well-log data and the seismic studies (Alcalde et al., 2013a,b; Quintà, 2013). The injection is projected to occur in the basal part of the Lower Jurassic carbonates at about 1500 m TVD (Fig. 2). The primary reservoir is constituted by a dolostone unit (upper part of Puerto de la Palombera Fm.) and an oolitic limestone unit (Sopeña Fm., Fig. 2). The reservoir has a thickness of more than 100 m and the porosity estimate, according to vintage well logs, ranges from 0% to 18% (Márquez and Jurado, 2011). From the 2D resistivity model a porosity value of between 9% and 17% was derived using Archie's Law (Ogaya et al., 2013).

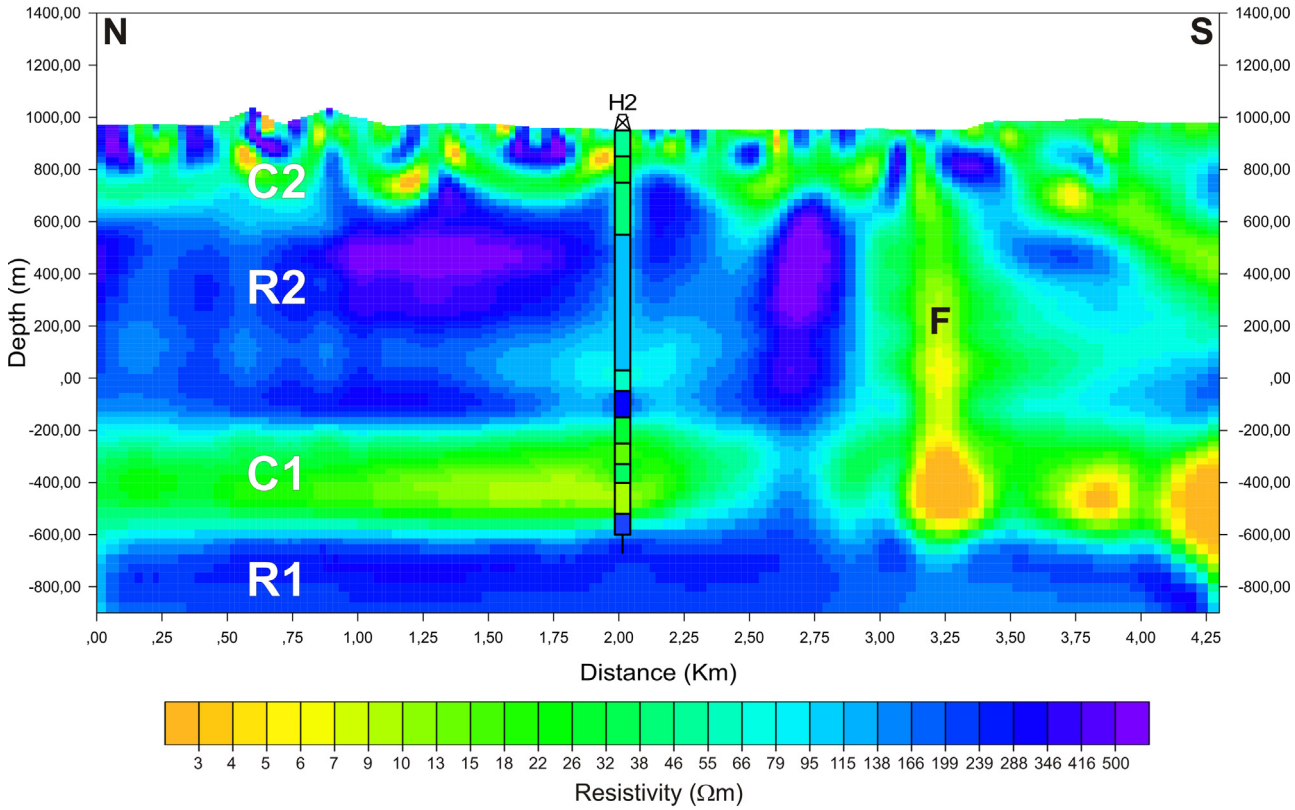

Fig. 3. 2D resistivity model of the MTD-profile data (reproduced from Ogaya et al., 2013). The four main layers of the resistivity distribution are (from bottom to top): R1, C1, R2 and C2. F indicates the fault region located in the southern part of the model. Superimposed is the 1D resistivity model of the H2 well. Depths are given in terms of metres above sea level (m.a.s.l.).

The primary seal comprises four black-shale levels interbedded in Lower Jurassic marls (Camino Fm., Fig. 2). A suitable secondary reservoir-seal system is represented by the intercalations of conglomerates, sandstones and shales from the Purbeck and Weald facies (Upper Jurassic-Lower Cretaceous).

The electrical behaviour of the different units is shown in Fig. 2 (inferred from the H2 well data; Ogaya et al., 2013). The primary reservoir is a saline aquifer and corresponds to the most conductive unit (10 Ωm in H2 well). The average electrical conductivity of the saline water is 47 mS/cm (a resistivity of 0.22 Ωm; Buil et al., 2012). The primary seal also has a conductive behaviour, whereas the secondary reservoir-seal system is resistive.

2.1. 1D models from the resistivity log-data

Fig. 1c shows the location of all drilled wells. H1, H2, H3 and H4 were drilled for oil exploration purposes (H1 and H2 in the late nineteen-sixties; H3 in 1991 and H4 in 2007) and their depths range up to 1769 m TVD. GW1, GW2 and GW3 are hydrogeological boreholes and were drilled recently (2012) to carry out groundwater studies; their depths range between 150 m and 405 m TVD (Benjumea et al., 2012). Following the procedures used in Ogaya et al. (2013) for the H2 well, where the resistivity log data were smoothed into the minimum number of layers required to describe the subsurface, an equivalent one-dimensional (1D) resistivity model was sought for each of the existing wells. These 1D models produce the same MT responses at the surface, as those ones obtained from forward modelling using the logged resistivities. Since the H4 well (drilled to a depth of 1610 m TVD) lacked resistivity log data, its 1D resistivity model was inferred using the H2-well data to correlate the different lithologies to electrical properties. It constitutes a good approximation as the two wells are located in the centre of the dome and, consequently, they are expected to show a similar pattern. The distance between the two wells is 707 m.

2.2. 2D resistivity model

The previous 2D resistivity model from the MTD profile in Fig. 1c (Ogaya et al., 2013) imaged a resistivity structure composed of four main layers (Fig. 3; all depths are given in terms of metres above sea level, m.a.s.l.): (i) R1 resistive bottom layer (below −600 m.a.s.l.) linked to Keuper facies; (ii) C1 conductive layer (below −200 m.a.s.l. and thickness up to 400 m) containing the primary reservoir and seal units; (iii) R2 resistive middle layer (between +700 m.a.s.l. and −200 m.a.s.l.) containing the secondary reservoir-seal system, and (iv) C2 conductive top layer (above +700 m.a.s.l.) linked to Upper Cretaceous materials. In the southern part of the model a fault region (labelled as F) was imaged that is related to the Ubierna Fault. The F structure revealed an important conductive fluid circulation along the fracture region.

3. Magnetotelluric method

A description of the MT method was given in Ogaya et al. (2013) and here is only briefly summarised. The MT method infers the electrical conductivity structure of the subsurface using the naturally occurring time variation of the EM field. EM waves propagate diffusively through the conducting Earth and their penetration depends on its period (T) and the electrical resistivity of the penetrated medium (ρ). The skin-depth ($\delta = 503\sqrt{\rho T}$ in SI units) is a reasonable estimate of the inductive scale length: the distance over which EM fields are attenuated to $1/e$ of their amplitudes at the Earth's surface in a uniform medium. Thereby, the longer the period, the deeper is the penetration depth.

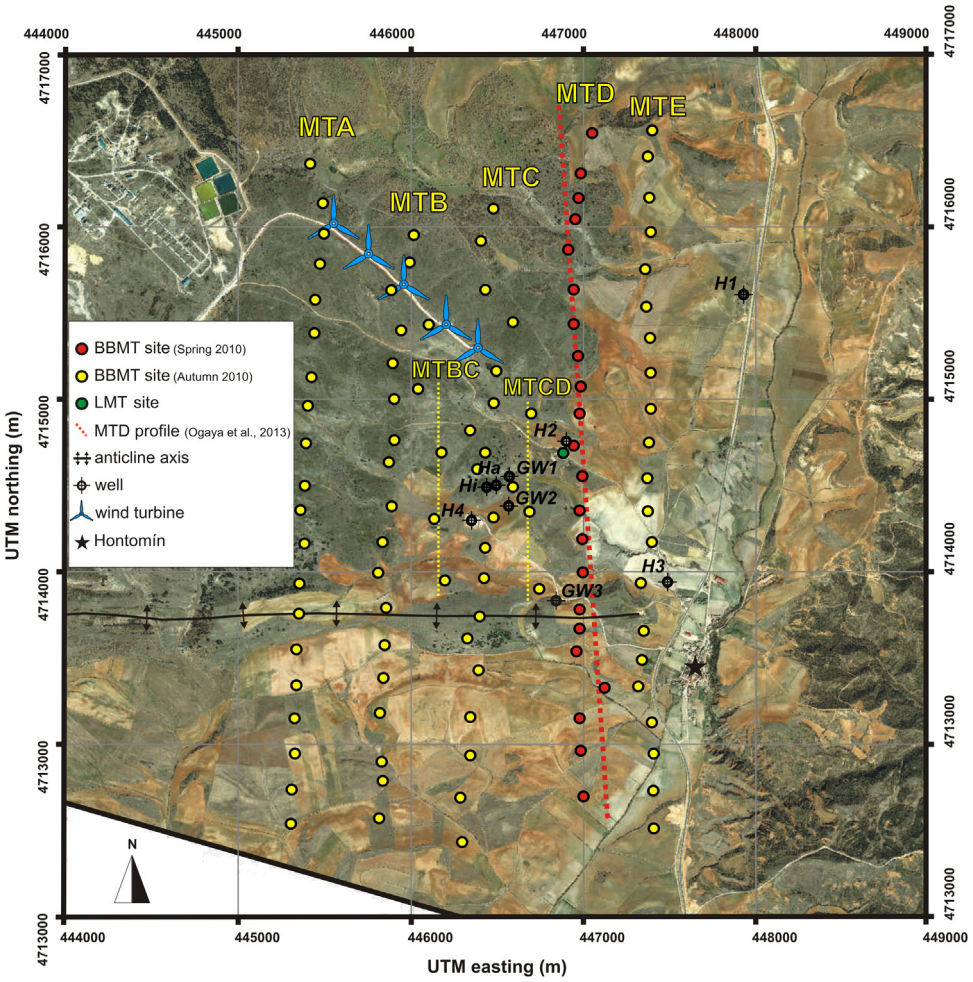

Fig. 4. Locations of the BBMT and LMT sites. In red, the BBMT sites collected in Spring 2010; in yellow, the BBMT sites collected in Autumn 2010 and in green, the single LMT site collected during a third phase of the fieldwork acquisition. Indicated are the acronyms of the profiles as well as the orientation of the 2D model presented in Ogaya et al. (2013; Fig. 3). Small yellow dotted lines indicated MTBC and MTCD profiles. Also shown are the positions of the wells and wind turbines (major EM noise source within the study area). (For interpretation of the references to colour in this figure legend, the reader is referred to the web version of this article.)

The orthogonal electric and magnetic field variations recorded at the Earth's surface are related to each other through the impedance tensor $Z_{ij}(\omega)$, function of oscillation frequency ω. From the impedance tensor are derived the MT response functions: apparent resistivity (ρ_{aij}) and phase (φ_{ij}). The form of this complex second-rank tensor is related to the dimensionality of geoelectrical structures. For that reason, a thorough dimensionality analysis of the MT data is necessary to determine which approach is more adequate: 1D, 2D or 3D. The dimensionality analysis yields information about the direction along which the electrical resistivity remains constant (geoelectric strike direction) and makes it possible to correct the MT data by detecting and removing most of the possible galvanic distortion effects. Nowadays, different approaches are commonly used: (i) Groom-Bailey distortion decomposition method for a regionally 2D geoelectrical subsurface (Groom and Bailey, 1989); (ii) analysis of the set of rotational invariants of the impedance tensor presented by Weaver et al. (2000), and (iii) the study of the phase tensor which relates the real and imaginary parts of the impedance tensor (Caldwell et al., 2004). For an extended description and comparison of the different existing methologies, see Jones (2012) in the recent book on MT by Chave and Jones (2012).

Different 3D MT inversion algorithms have been developed in the last years although 3D inversion requires further development and understanding of the advantages and limitations. For a test and comparison of the current available codes see the compilation of Miensopust et al. (2013). In this Hontomín work, three different 3D inversion codes were used: the code described by Mackie and Madden (1993) subsequently developed and implemented by Geosystem (called Geosystem code hereafter); WSINV3DMT (Siripunvaraporn et al., 2005) and ModEM (Egbert and Kelbert, 2012). The first one is a commercial code and uses a truncated non-linear conjugate gradient approach. The second, WSINV3DMT, is based on a data-space variant of the Occam's approach. Finally, ModEM, is a modular system of computer codes for different EM problems and the inversion algorithm is also based on a non-linear conjugate gradient scheme. For a comprehensive explanation about 3D inversion and modelling, see the following reviews: Avdeev (2005), Börner (2010) and Siripunvaraporn (2012).

4. Magnetotelluric data and dimensionality analysis

The EM characterisation of the Hontomín site was divided into two stages: first, a 2D acquisition was carried out in Spring 2010 (profile presented in Ogaya et al., 2013 and renamed to MTD in this work; red dots in Fig. 4), and then, a 3D acquisition was undertaken in Autumn 2010 (yellow dots in Fig. 4). Eighty-seven new broadband magnetotelluric (BBMT) sites were acquired in the second fieldwork to complement the 22 made in the first fieldwork, making a total of 109 BBMT sites on a grid covering

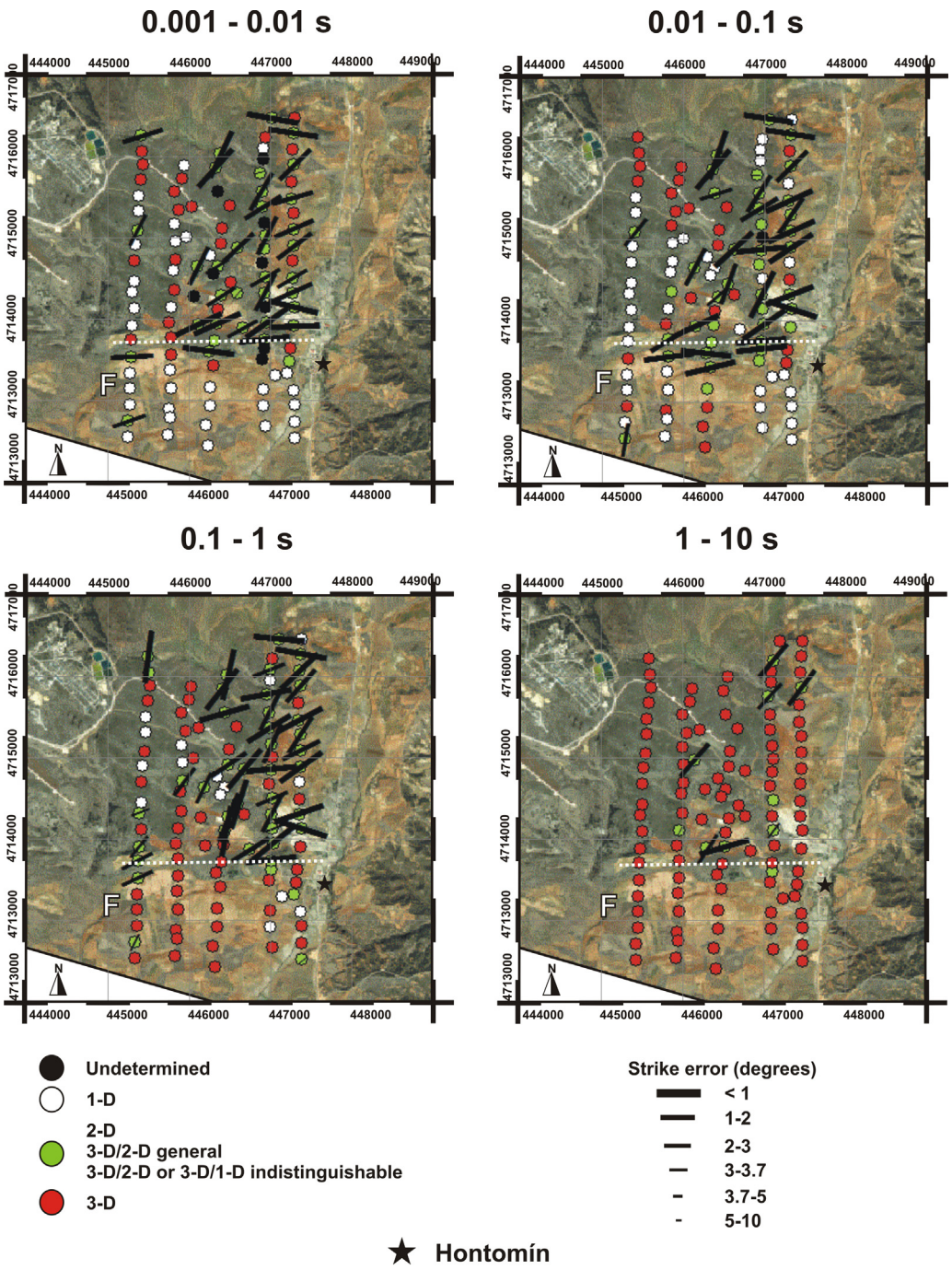

Fig. 5. Map of dimensionality analysis using the WALDIM code for four different period ranges: 0.001–0.01 s, 0.01–0.1 s, 0.1–1 s (primary reservoir-seal system) and 1–10 s. White dots infer 1D geoelectrical structures. Green dots group all inferred 2D cases: purely 2D case, 3D/2D general case with 2D structures affected by galvanic distortion and indistinguishable cases 3D/2D and 3D/1D, where the galvanic distortion makes impossible to determine the strike direction. Red dots designate the inferred 3D cases. Geoelectric strike is indicated by black lines of length inversely proportional to its error. The white dotted line shows the approximate north-border of the F region. The location of Hontomín village is indicated. (For interpretation of the references to colour in this figure legend, the reader is referred to the web version of this article.)

an approximately extent of $3 \times 5\,km^2$. The data were mainly organised along five NS profiles: MTA, MTB, MTC, MTD and MTE (Figs. 1c and 4). To refine the grid in the injection area (Hi region), two smaller NS profiles were acquired: MTBC and MTCD (indicated with yellow dotted lines in Fig. 4). All profiles were perpendicular to the EW trend of geological structures and crossed the EW fault imaged in the previous 2D resistivity model (F fault, Fig. 3). The length of each profile was around 4 km and the average distance between them was approx. 500 m. The stations were distributed on 200 m intervals along the profiles. The instrumentation consisted of Metronix ADU06, Metronix ADU07 and Phoenix V8 recorders with induction coil magnetometers and NaCl-type electrodes with a typical electrode line length of 70 m. The *x*-axis was oriented in the magnetic NS direction with the positive direction pointing to the north, and the *y*-axis in the EW direction pointing to the east. The data were acquired in the period range of 0.001–100 s (1000–0.01 Hz frequency range). The processing and quality control of the new data was the same as the one described in Ogaya et al. (2013). The data were recorded during 24 h and a permanent remote reference (RR) station was placed 20 km away from the H2

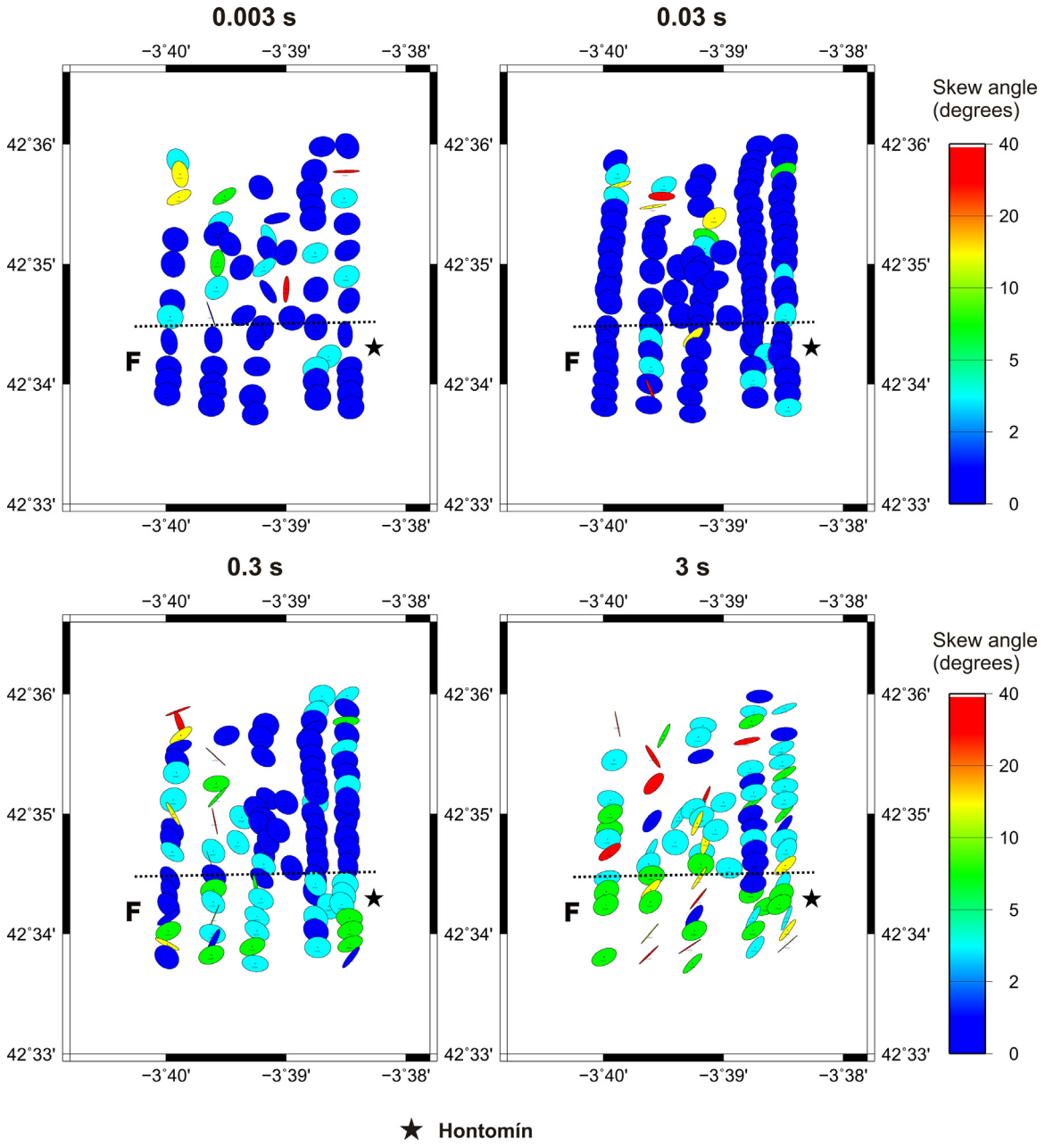

Fig. 6. Phase tensor at each site for four different periods: 0.003 s, 0.03 s, 0.3 and 3 s. The azimuth of the semi-major axis corresponds to the strike direction and the difference between the length of the semi-major and semi-minor axis gives an estimate of the dimensional complexity of the geoelectrical structure (i.e., a circle matches with the 1D case). The colour of the ellipse shows the skew angle β which indicates the 3D character of the resistivity distribution ($\beta = 0$ for a 2D case). As the plot corresponds to four single periods, some of the sites do not have data. The black dotted line shows the approximate north-border of the F region. The location of Hontomín village is indicated.

well to improve the quality of the longest periods (same location as in Ogaya et al., 2013). Moreover, BBMT acquisition was designed in a manner that at least 4 stations were recording at the same time to minimise the effects of the EM noise using also local multiple RR techniques. During a third phase of fieldwork acquisition, a single long period magnetotelluric (LMT) data set was collected to obtain information about the deeper structures (green dot in Fig. 4). The LMT data were acquired in the period range of 16–20000 s using a LEMI system (Lviv Centre of Institute of Space Research).

Robust processing codes employed to derive the BBMT responses were the ones that demonstrated their validity in the previous 2D survey (Egbert and Booker, 1986). The RR technique (Gamble et al., 1979) was used at all stations to improve the quality of the BBMT data between 0.5 and 10 s. The implementation of the local RR technique was crucial for improving the data collected near the wind turbine region (shown on Fig. 4) and consisted of undertaking RR with sites located in the southern part of the study region (less noisy area). At periods exceeding 10 s, ambient noise dominated the natural signal and consequently, the studies were undertaken in the period range of 0.001–10 s (1000–0.1 Hz). The LMT data were processed using Birrp.5 (Chave and Thomson, 2004).

The dimensionality analysis of the acquired MT data was evaluated using (i) the WALDIM code of Martí et al. (2009) based on the Weaver impedance invariants (Weaver et al., 2000), and (ii) studying the phase tensor (Caldwell et al., 2004). Fig. 5 shows the results obtained using the WALDIM code at each site for four different period ranges: 0.001–0.01 s, 0.01–0.1 s, 0.1–1 s and 1–10 s. The assigned error level in the impedance components was of 5% and the thresholds set for the invariants were: $\tau = 0.19$ for invariants I_3–I_7 and $\tau_Q = 0.10$ for invariant Q. For short periods (shallow

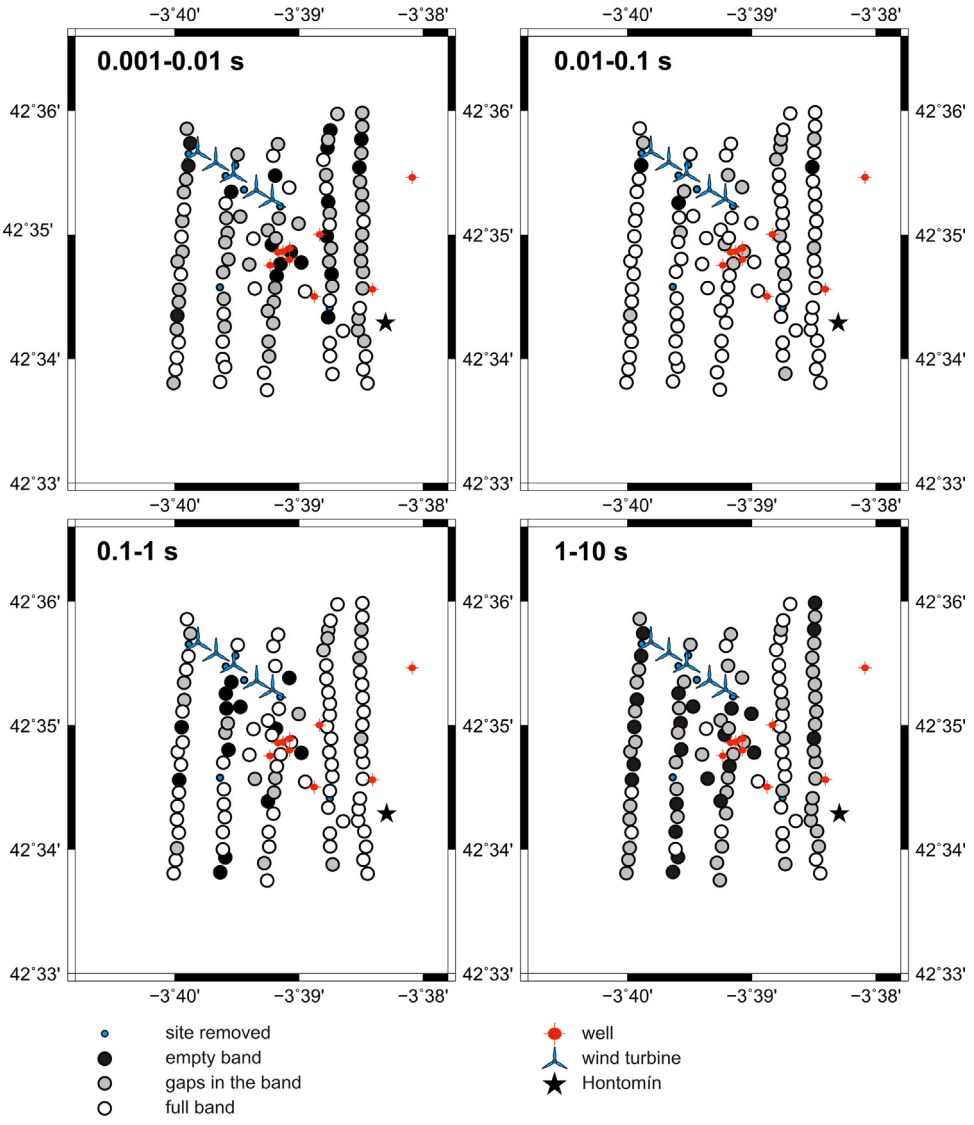

Fig. 7. Quality of the BBMT data. White big dots indicate sites with information in the whole range of periods whereas large black dots indicate sites without any data in the range. Intermediate cases with gaps in the period range are indicated by grey dots. Small blue dots represent the excluded noisy sites. The positions of the wells and the wind turbines, main EM noise source of the study area, are indicated. (For interpretation of the references to colour in this figure legend, the reader is referred to the web version of this article.)

depths), the results indicate 1D/2D conductivity, being mainly 1D in the F region (in the south). On the contrary, when increasing the period (equivalent to increasing the depth of penetration), geoelectrical structures become more complex and present a 3D behaviour.

Fig. 6 plots the phase tensor at each site for four different periods: 0.003 s, 0.03 s, 0.3 and 3 s. As the phase tensor is independent of the electric effects of galvanic distortion, this analysis aimed to determine if there existed an important galvanic distortion in the WALDIM results and, in this way, to estimate to what extent this distortion was perturbing the data. Results indicate that the geoelectrical structure becomes more complex with increasing the period, as showed for the WALDIM analysis.

Thereby, the dimensionality analysis corroborated that a 3D inversion of all the BBMT data set was necessary to avoid misinterpretation of the geoelectrical structure of the Hontomín URL at periods longer than 0.1 s (Ogaya et al., 2012). Moreover, it was concluded that galvanic distortion in the study area was small, since results of the phase tensor study were consistent with the ones obtained using the WALDIM code.

The internal self-consistency of the *XY* and *YX* BBMT data apparent resistivity and phase curves was analysed through D^+ model solutions (Parker, 1980; Parker and Whaler, 1981). This method facilitates detecting and removing outliers and noisy points by analysing the physical validity of the MT responses. Thus, using an estimated data error of 10% for the apparent resistivity and phase, less than 30% of the BBMT data was discarded. This fraction included data from all sites in the range of 10–100 s – the noisy region. Seven BBMT sites were excluded from the inversion because they were considered too noisy with a high and linearly polarised signal (Escalas et al., 2013). Almost all of them were near the wind turbine region. Fig. 7 summarises the quality of the BBMT data, indicating: complete period bands (white); period bands with gaps (grey); empty period bands (black) and excluded sites (blue). Most of the grey cases correspond to curves with shortest periods longer than 0.001 s and/or longest periods shorter than 10 s. This defines the data set for the 3D inversion.

For the data set for the inversion, the minor static effects of galvanic distortion were dealt prior to the inversion using the available

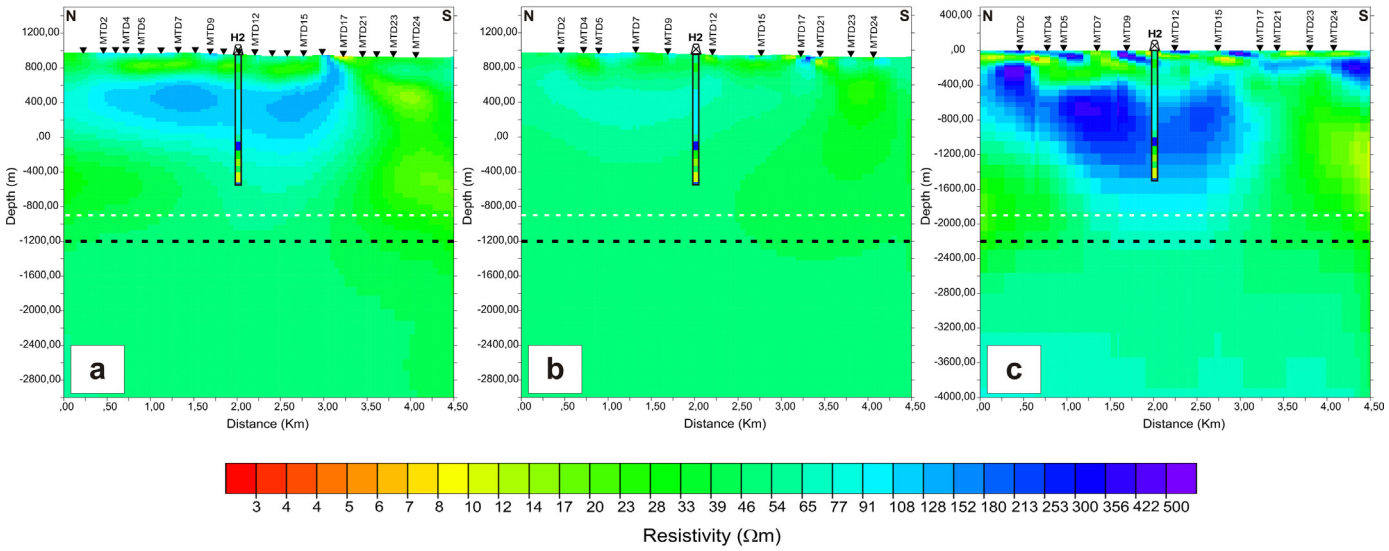

Fig. 8. Equivalent section to the MTD profile modelled in Ogaya et al. (2013) for each of the three initial inversions from a uniform 50 Ωm halfspace: (a) model Ø, (b) ModEM and (c) WSINV3DMT. The black dashed line indicates the approximate depth at which the resistivity increase is observed (depths are given in terms of m.a.s.l. in (a) and (b) cases, and in terms of TVD in (c) case). The white dashed line indicates the bottom of the 2D model shown in Fig. 3. Superimposed appears the 1D resistivity model of the H2 well (Fig. 2a). BBMT sites are marked by black triangles.

resistivity log data to fix the resistivity values at shallow depths. In general terms, the static shift corrections were smaller than a logarithmic decade. Static shift correction could imply a loss of information but related to near surface structures that are not the target of this study.

Giving the predominant 3D behaviour of the geoelectrical structures for periods longer than 0.1 s, the diagonal components of the impedance tensor were considered for the inversion. The importance of including the diagonal components in 3D inversion was recently emphasised by Kiyan et al. (2014). For the shortest periods, the amplitude of the apparent resistivity of the diagonal components at most sites is two to three decades smaller than the off-diagonal components. However, for the longest periods, the difference of amplitude between the diagonal and off-diagonal components is less than a decade. In general, the diagonal component data are of reasonable quality and their apparent resistivity and phase curves are not scattered; their amount of error is relatively low (see supplementary Figs. S1–S17).

Supplementary material related to this article can be found, in the online version, at doi:10.1016/j.ijggc.2014.04.030.

5. 3D inversion of the MT data

5.1. General aspects (setup)

The work flow for 3D inversion consisted in improving a preliminary model provided by Geosystem (Mackie and Madden, 1993; model Ø hereafter; Fig. 8a) using the ModEM code (Egbert and Kelbert, 2012). WSINV3DMT (Siripunvaraporn et al., 2005) was also used to undertake some testing and to study the consistency of the models.

The topography of the study area is relatively gentle: elevations range from 919 to 1040 m.a.s.l. with the highest ones to the NW area (wind turbine region). As the target regions are located at depths below the surface no greater than 1800 m TVD, it was considered important to incorporate topography in the model. To

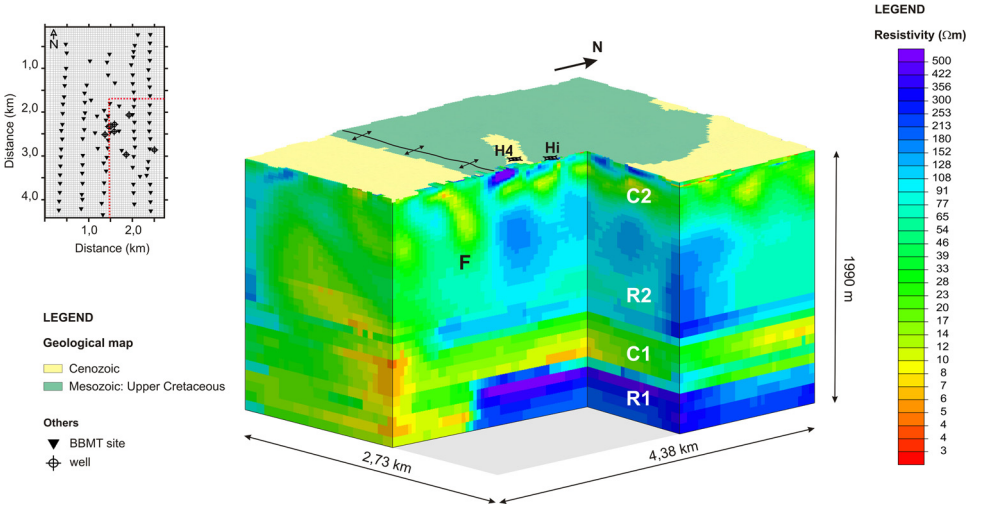

Fig. 9. Final 3D resistivity model of the Hontomín URL subsurface with a cutout (red dotted lines indicate the location of the NS and EW cuts). The geological map of the study area is shown and the positions of the wells and BBMT sites are marked. The F region and the main resistivity layers (R1, C1, R2 and C2) are also indicated. Depths are given in terms of m.a.s.l. (For interpretation of the references to colour in this figure legend, the reader is referred to the web version of this article.)

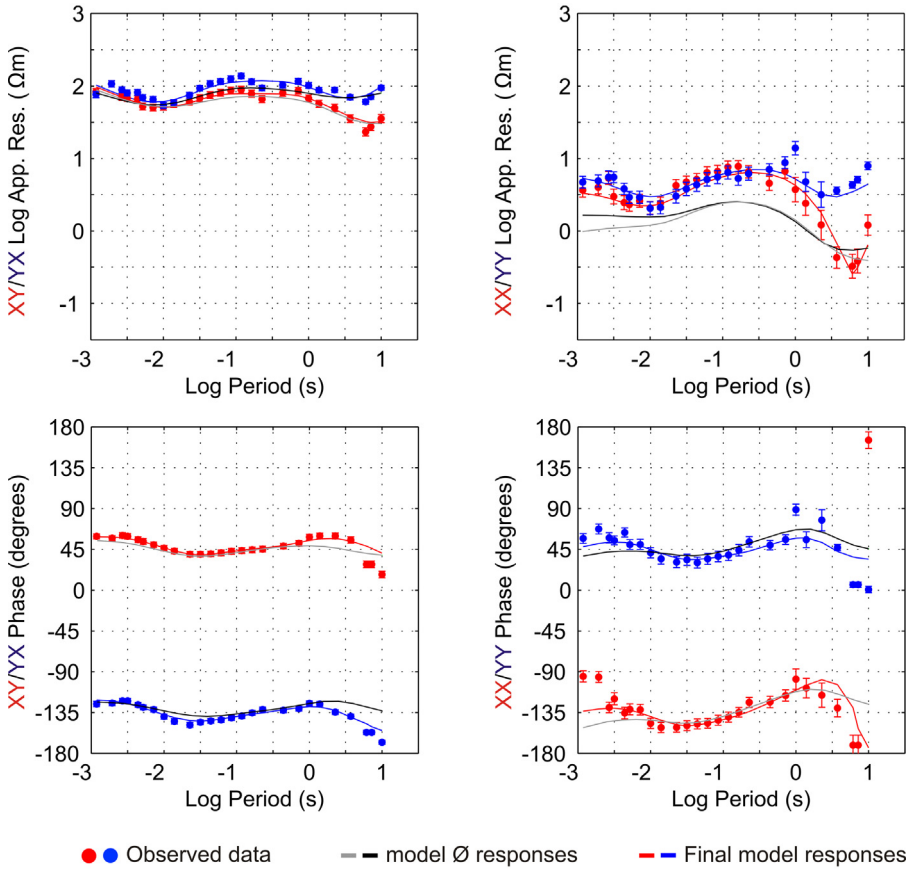

Fig. 10. Responses of the model Ø and the final 3D model at site MTD7.

avoid sharp boundaries between the air and earth cells, a smooth topography was implemented. The mesh was a $73 \times 114 \times 113$-layer grid including topography for Geosystem and ModEM's cases (an approximate model extension of $61 \times 63 \times 54\,km^3$). For WSINV3DMT's test cases, the mesh was a $52 \times 68 \times 60$-layer grid but excluded topography (an approximate model extension of $70 \times 72 \times 52\,km^3$).

The final inversions were undertaken using up to 29 periods of the full impedance tensor for the 102 BBMT sites in the range of 0.001–10 s. The error floor set was 5% for the off-diagonal components (2.865 degrees for the phases and 10% for apparent resistivity) and 10% for the diagonal components (5.73 degrees and 20% for the apparent resistivity). Missing data periods were interpolated and included but had assigned large error bars.

The models were run on the Stokes cluster of the Irish Centre for High-End Computing (ICHEC) and on the Mallet and Lehmann clusters from Dublin Institute for Advanced Studies (DIAS). The main aspects of the inversion process are detailed below.

5.2. Initial 3D inversions

Some initial inversions were run using ModEM and WSINV3DMT codes to validate the initial model Ø used and to assess its geological consistency. The initial model was for both cases a halfspace of 50 Ωm (as for Geosystem's inversion) which agrees with the average resistivity value of the H2 well log data (Fig. 2). The inversions were undertaken using the full impedance tensor. However, in order to assure the convergence of these initial models, first iterations were undertaken using only 50 sites uniformly distributed and covering all the area, and the off-diagonal components. Once the main structures were defined, more sites and components were included in the inversion. The greater was the amount of data incorporated to the inversion, the greater was the definition and resolution of the imaged structures. As was also seen in Ingham et al. (2009), the resistivity structure obtained from the first inversions with only a small number of sites was basically the same as that obtained with the whole data set, i.e., the existence of conductivity structures is a robust first-order feature in the data set. The data fit was better doing a correction of the static shift prior to the inversion.

Fig. 8 shows a section of the 3D model coincident with the MTD 2D profile modelled in Ogaya et al. (2013), for each of the three initial inversions from a uniform halfspace: (a) model Ø, (b) ModEM and (c) WSINV3DMT. The 3D models fit the data with an RMS misfit of 1.36, 2.25 and 2.05, respectively. Despite the discrepancies related to topography, as it is included in (a) and (b) cases and not included in (c) case, the results from the initial 3D inversions confirmed that the three models are equivalent in the sense that all of them recovered the same main resistivity features. Moreover, the obtained electrical resistivity distribution resembles the one imaged in the previous 2D model (Ogaya et al., 2013; Fig. 3), proving the geological consistence of the models. Thus, it was considered appropriate to define the model Ø as the initial model for the subsequent inversions with the ModEM code.

Nevertheless, comparing the obtained models to both the 2D model (Ogaya et al., 2013; Fig. 3) and the resistivity well logs existing in the area, it was noticed that none of the inversions recovered the resistive structure located at 1600 m TVD (R1 in Fig. 3). The models only imaged a slight increase in the resistivity at around 2200 m TVD (at −1200 m.a.s.l. for models with topography). This depth is indicated by a black dashed line in Fig. 8. Therefore, the fitting of the deepest part needed to be improved.

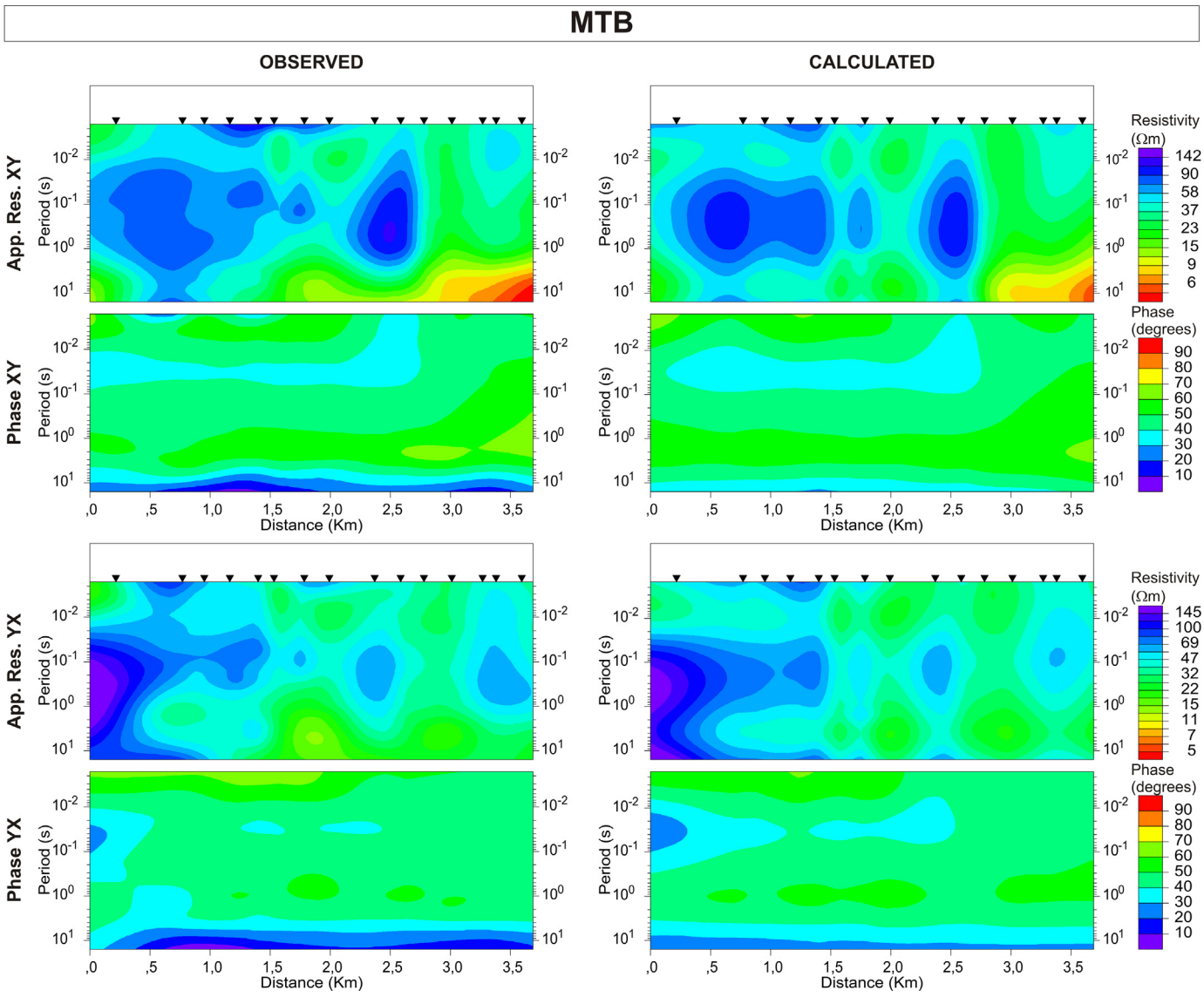

Fig. 11. Pseudosections of MTB profile: apparent resistivity and phase for observed data and model responses. The positions of the BBMT sites are marked by black triangles.

To address this issue, several inversions using the ModEM code were carried out for different period bands: the shortest periods were fitted first and then, the longest periods were inverted fixing the upper part of the model. The fit of the shortest periods was improved but improvement did not occur in the same manner with the longest ones. Through 3D synthetic studies it was corroborated that the primary system (primary reservoir and seal) MT responses were principally in the range of 0.1 to 1 s, as was previously affirmed by Ogaya et al. (2013). In this way, the data collected at the Hontomín site were imaging the deepest resistive layer R1 but a non-constrained 3D inversion was unable to recover the layer. The inversion needed to be better constrained at depth in order to resolve the bottom of the main reservoir and recover the R1 layer.

5.3. Final 3D resistivity model

For the final model, a more constrained inversion was carried out incorporating new information for the initial model. As has been discussed in other publications (e.g., Piña-Varas et al., 2013), an appropriate selection of the initial model is sometimes necessary to produce a meaningful model from a geological point of view. Thus, according to the existing resistivity-log data and the geoelectrical structure imaged in Ogaya et al. (2013), included in the initial model was a 25 Ωm conductive layer at approximately −220 m.a.s.l. and a resistive layer of 200 Ωm between −600 and −2000 m.a.s.l. Data from the single LMT site were incorporated to the inversion (period range of 10–340 s; see supplementary Fig. S12).

The final 3D model fits the data with an RMS misfit of 1.71 (Fig. 9). Fig. 10 plots the responses of model Ø and the final model at site MTD7 showing the improvement of the fit at the longest periods and also for the diagonal components. The data and model responses at all sites are plotted in supplementary Figs. S1–S17. Comparisons between data and final model responses for the off-diagonal components are shown in Fig. 11 for the MTB profile and in Fig. 12 for the MTD profile (approximate limits of the URL). The misfits of the other profiles are shown in supplementary Figs. S18–S22. As is illustrated, the fit is satisfactory and the residuals are random and small; no significant feature in the data is unexplained.

Supplementary material related to this article can be found, in the online version, at doi:10.1016/j.ijggc.2014.04.030.

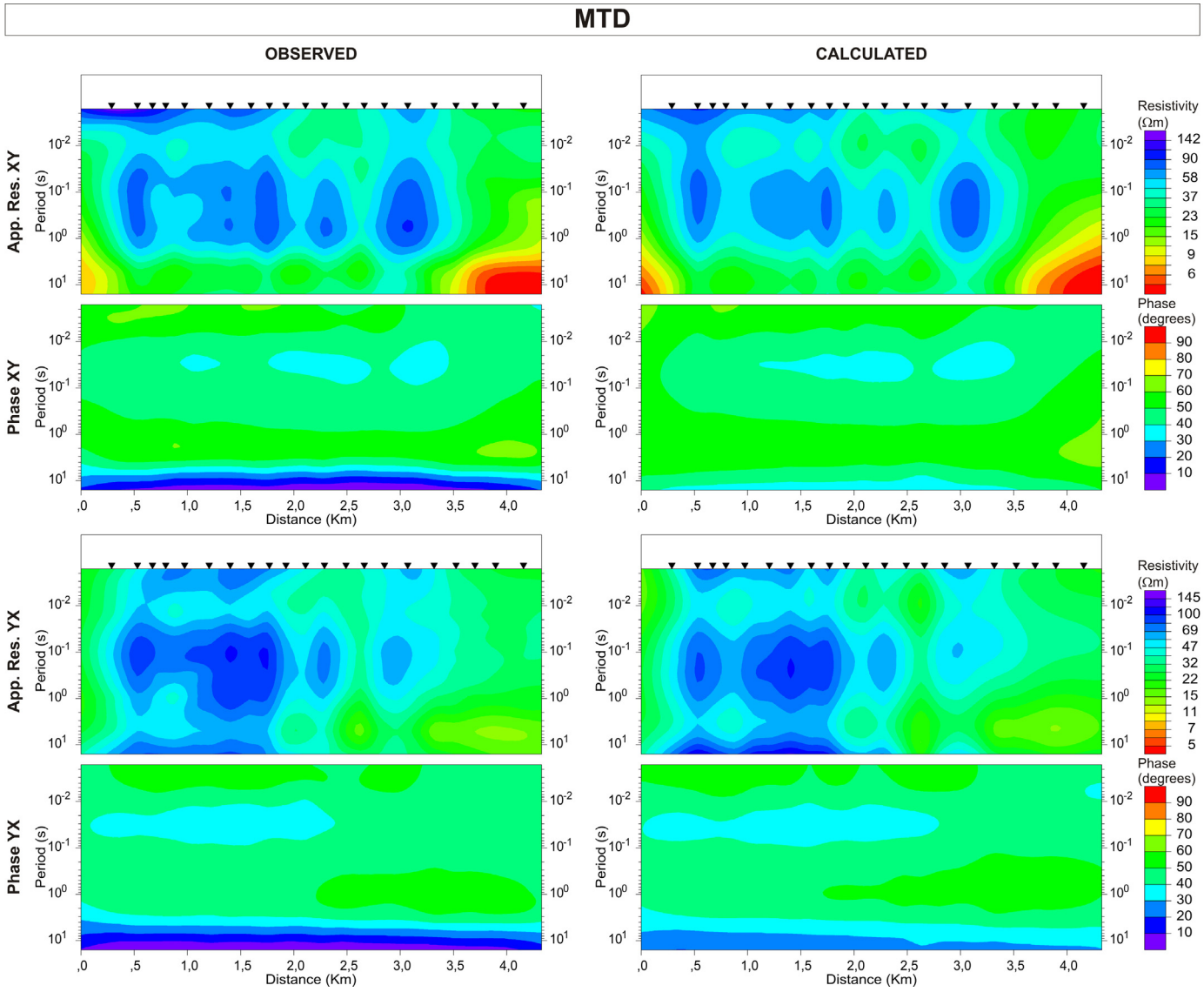

Fig. 12. Pseudosections of MTD profile: apparent resistivity and phase for observed data and model responses. Differences with pseudosections shown in Ogaya et al. (2013) are because the MT data were not rotated in this work. In Ogaya et al. (2013) the data were rotated 4° W; the transverse magnetic (TM) mode was identified with *XY* polarisation and the transverse electric (TE) mode, with *YX* polarisation. The positions of the BBMT sites are marked by black triangles.

The geoelectrical structure from near surface to −900 m.a.s.l. is an alternation of conductive and resistive layers (from bottom to top; Figs. 13–16): R1, C1, R2 and C2. The location of the tops and bottoms of the layers, as well as their thicknesses, vary along each profile and between profiles. The southern part of the model (F region) is mostly conductive, being much more conductive in the eastern part than in the western part. Through non-linear-sensitivity tests (e.g., Ledo and Jones, 2005) the most conductive eastern part of the F fault region (region 1 in Fig. 13b) and the continuity of the R2 layer in the southern part of the model (region 2 in Fig. 13b) were both evaluated. The tests consisted of replacing the resistivity values of these regions by their surrounding resistivity value: 30 Ωm for region 1 and 200 Ωm for region 2. In both cases, the difference between the responses of the final model and the modified one was greater than the error floor imposed in the MT data for the inversion (results for region 1 in Fig. 17 and results for region 2 in Fig. 18). In this way, that conductive region 1 is required by sites located in the southern part of the model, mainly the ones in the MTD and MTE profiles, was corroborated. This conductive feature was also imaged in the 2D model (Fig. 13a). Results from region 2 indicate that there is no continuity of the R1 layer in the southern region of the model (Fig. 18).

6. Comparison with other EM studies

6.1. MTD profile

Fig. 13 shows (a) the 2D model and (b) its equivalent section from the final 3D model. The topography of the two models is slightly different because of the smoothing of the 3D topography. The models are consistent and only relatively minor differences are apparent. In the 3D model: (i) R1 layer is more resistive under sites MTD14-MTD15 and does not extend under sites MTD21-MTD24; (ii) the most conductive portion of C1 layer is located in the north and there is not a clear discontinuity of the layer because of a more resistive area under sites MTD14-MTD15; (iii) in general terms, R2 range of resistivity values is narrower, and (iv) C2 layer contains less scattered bodies. Regarding the F region, its structure is less

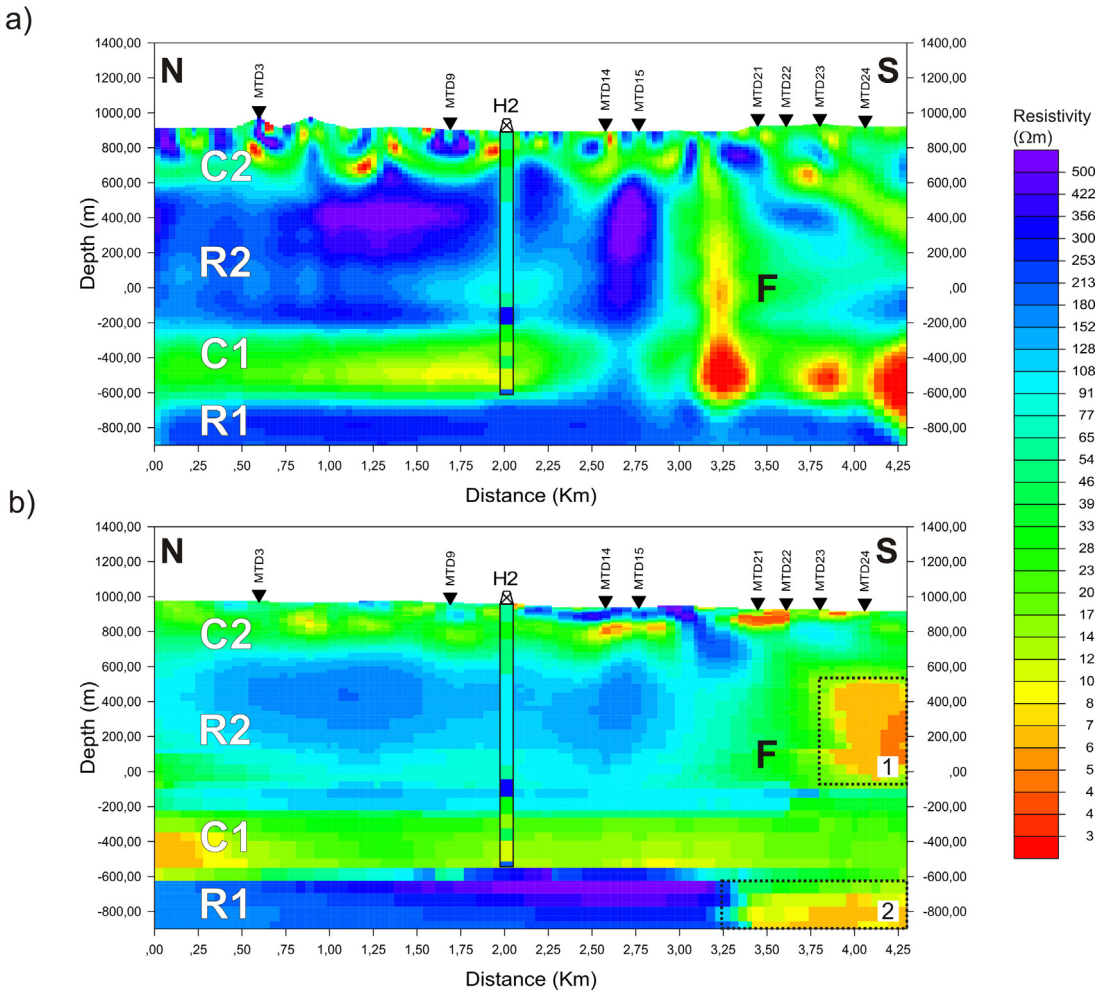

Fig. 13. (a) 2D model of the MTD profile (Ogaya et al., 2013) and (b) its equivalent section of the final 3D model. The same resistivity colour scale is used for both models. The main resistivity layers (R1, C1, R2 and C2) and the F region are indicated. The 1D model provided by the resistivity-log data of the H2 well is superimposed and BBMT sites are marked by black triangles. The differences in topography are apparent because it was defined on a smoother surface for the 3D model. Black dotted lines indicate the two more conductive regions studied through non-linear-sensitivity tests: region 1 (Fig. 17) and region 2 (Fig. 18). Depths are given in terms of m.a.s.l.

well defined. In none of the models (neither the 2D nor the 3D) does the F fault seem to outcrop.

The major discrepancies are observed in the deepest structures (R1 and C1 layers). These structures are located in the period range of 0.1–10 s (Ogaya et al., 2013) which is the band where the data are not purely 2D and some 3D effects are observed (Figs. 5 and 6). The observed differences are therefore concluded to be mainly because of two reasons: the greater smoothness of the 3D models, primarily due to larger cell sizes, and the possible influence of 3D structures in the previous 2D inversion.

6.2. Correlation with resistivity log data

Fig. 14 shows three sections (profiles I, II and III) that cut the resulting 3D model by the existing H1–H4 wells. The simplified resistivity-log data of each well correlate well with the 3D model. The main differences are noticed for the H4 well which is reasonable since its 1D resistivity model was derived from the H2 well log data and the H2 well is located 707 m away. Likewise, the structure of the upper part of the model agrees with the 1D model derived from the GW wells.

Correlation of the final 3D model with the resistivity log data show that discrepancies are not significant, neither for the H wells nor for the GW wells. Thus, it was seen that for this case study, the correction of the static shift prior to the inversion provided accurate results.

7. Interpretation: 3D geoelectrical baseline model

Resistive layer R1

R1 is the deepest layer imaged in the 3D model. Synthetic studies showed it was mainly sensed at periods around 1 s. The top of this layer is shallowest (−552 m.a.s.l.) in the centre-eastern part of the model under profiles MTC, MTD and MTE (Fig. 15 h). The layer is also more resistive in that region (up to 1000 Ωm; Fig. 14). There is not a continuity of this layer in the southern region of the model (Fig. 13).

The R1 layer is interpreted as the Upper Triassic unit (Keuper facies). This unit is constituted by a succession of dolomites, anhydrites, and salt, which could explain its high resistivity. It is an impermeable layer that may constitute a suitable bottom seal for the main reservoir.

Conductive layer C1

The C1 layer is sensed in the period range of 0.1–1 s. The top of the layer is approximately at −216 m.a.s.l. (Fig. 15f). It has a

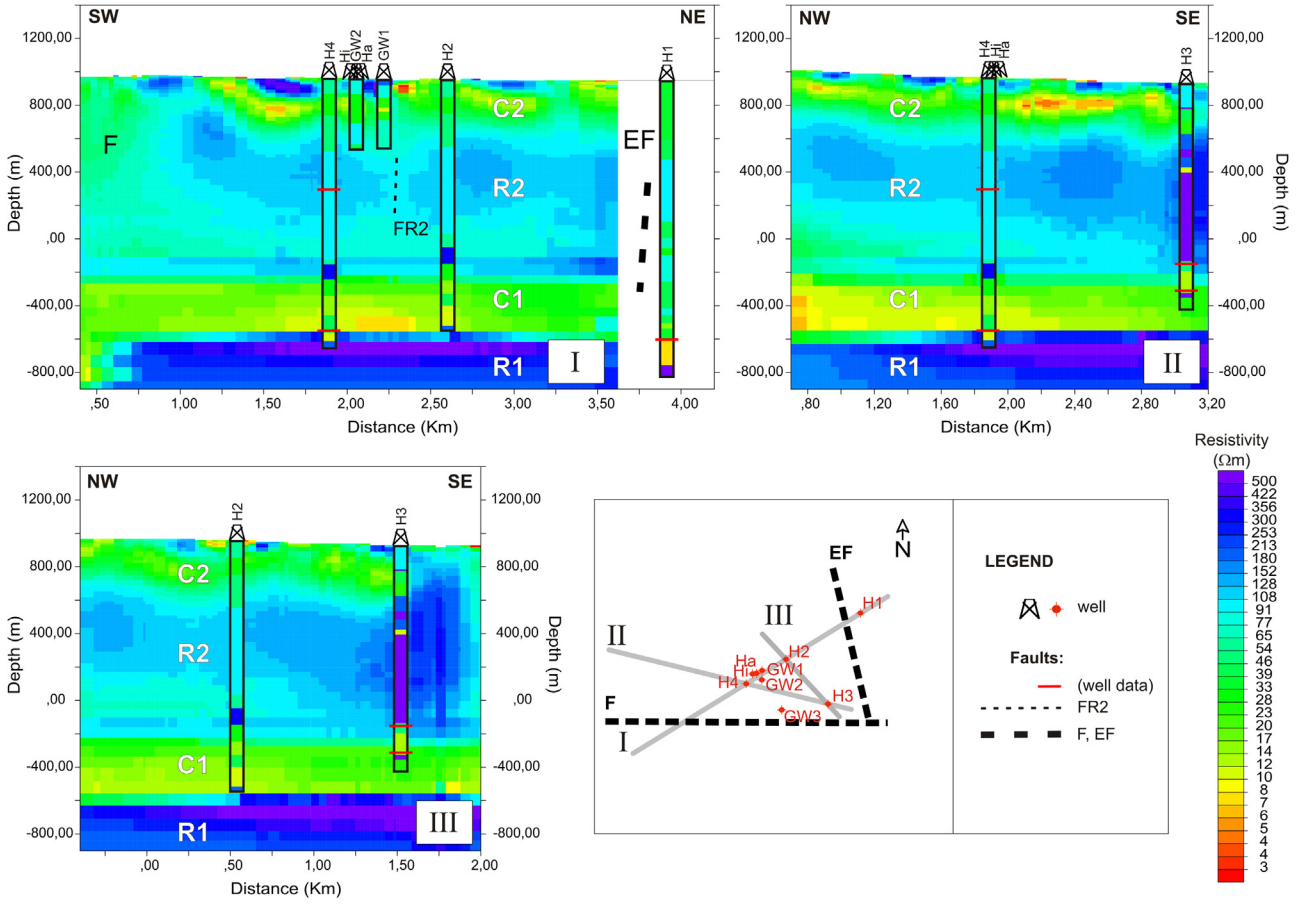

Fig. 14. Three sections (I, II and III) cutting the final 3D model by the existing wells. The main resistivity layers (R1, C1, R2 and C2) and the F and EF fault regions are indicated. Possible FR2 fracture regions and faults that cross the H wells according to well data, are also specified. The 1D resistivity models derived for each well (simplified resistivity-log data) are superimposed. Depths are given in terms of m.a.s.l.

dome-like structure with its axis situated in the injection area. The slope of the north flank is less steep and the dome seems to be elongated to the NW (Fig. 15f and g). The extension of the dome crest in this layer is about $1 \times 1\ km^2$.

The C1 layer contains Jurassic rocks according to the well log data. The main reservoir and seal units are interpreted to be located within it. The saline aquifer (main reservoir), is linked to the most conductive region inside C1, a 7–14 Ωm region labelled as C1a in Fig. 15g. The top of this most conductive layer is located around −400 m.a.s.l. The overlying primary seal also features a conductive behaviour, probably because of its marly composition (marlstones and black shales).

Resistive layer R2

R2 is the thickest layer within the model. The top of this layer is shallower in the NW part of the model, where is located at approximately 700 m.a.s.l. (Fig. 15b). R2 is interpreted as the upper part of Jurassic (upper part of the Dogger) and Early Cretaceous (Weald and Purbeck facies and Escucha Fm.) units. The secondary reservoir-seal system would be contained within the R2 layer.

Analysing the layer from bottom to top, one can deduce the possible evolution of the dome structure.

(i) The bottom of the R2 layer is defined by a more resistive sublayer of up to 130 Ωm and approximately 100 m thickness (Figs. 14 and 15e). According to the lithological information provided by the different wells, this increase in resistivity may be explained by a slightly increase on limestone content. In Fig. 15e is observed a less resistive region (below 100 Ωm) in the centre of R2, around the locations of the wells, which agrees with the dome-shape observed for the C1 layer.

(ii) Upwards, there exists a displacement of the dome crest to the east. At 177 m.a.s.l. (Fig. 15d), the crest of the dome seems to be located in the surroundings of the H2 well.

(iii) In the overlying layers (Fig. 15c) the resistive dome (resistivity values up to 220 Ωm) moves to the NW of the model. Consequently, at around 700 m.a.s.l. (Fig. 15b), the crest of the dome appears to be imaged in the NW region.

The R2 layer seems to be more conductive in the NW part of the model but this aspect may not be due to a geological explanation. As the quality of the data was lower in that region (wind turbine region; see Fig. 7), the error bars were larger. Thus resolution is poorer and naturally the smoothness constraint drives resistive regions to the lowest possible values they can take.

Conductive layer C2

The C2 layer is the surficial part of the model, i.e., the topmost layer. According to the well log data, it contains the Upper Cretaceous and Cenozoic materials that dominate the surface of the study area. The clear limit between the R2 and C2 layers (Figs. 13 and 14) is marked by the top of the Utrillas Fm. The R2 layer emerges in C2 (EW resistive body in Fig. 15a) due to the presence of the F region.

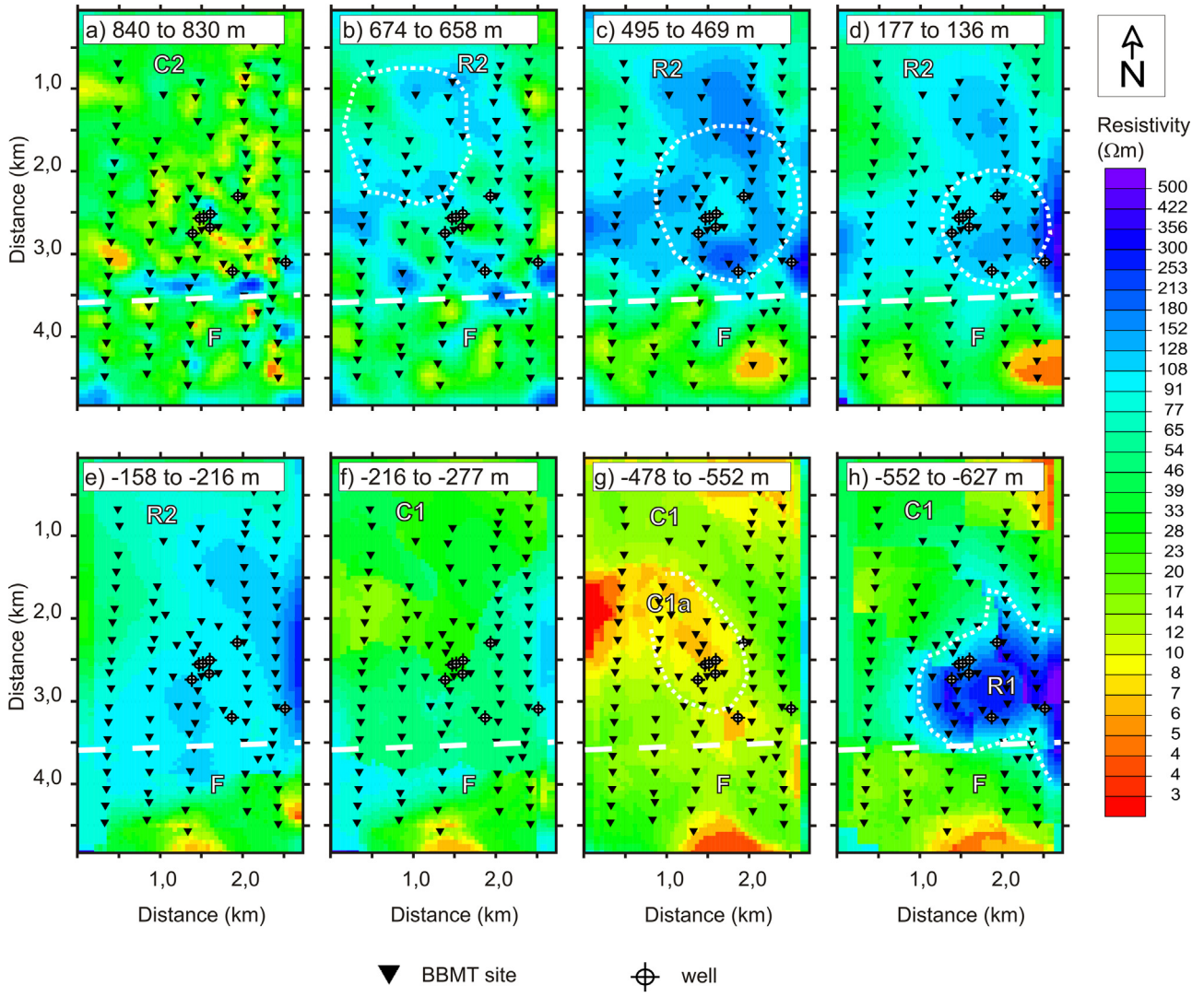

Fig. 15. Z-slices of the model from top (a) to bottom (h), with depths indicated in each sub-plot. The main resistivity layers (R1, C1, R2 and C2) and the F region are indicated. EW white dashed line indicates the approximate north-border of the F region. From bottom to top (depths given in terms of m.a.s.l.): (h) top of the R1 layer; (g) main reservoir C1a (saline aquifer); (f) top of the C1 layer; (e) bottom of the R2 layer; (d), (c) and (b) evolution of the R2 layer's dome structure and (a) C2 layer and bend of the R2 layer due to the presence of the F region. See text for more information about the white dotted lines.

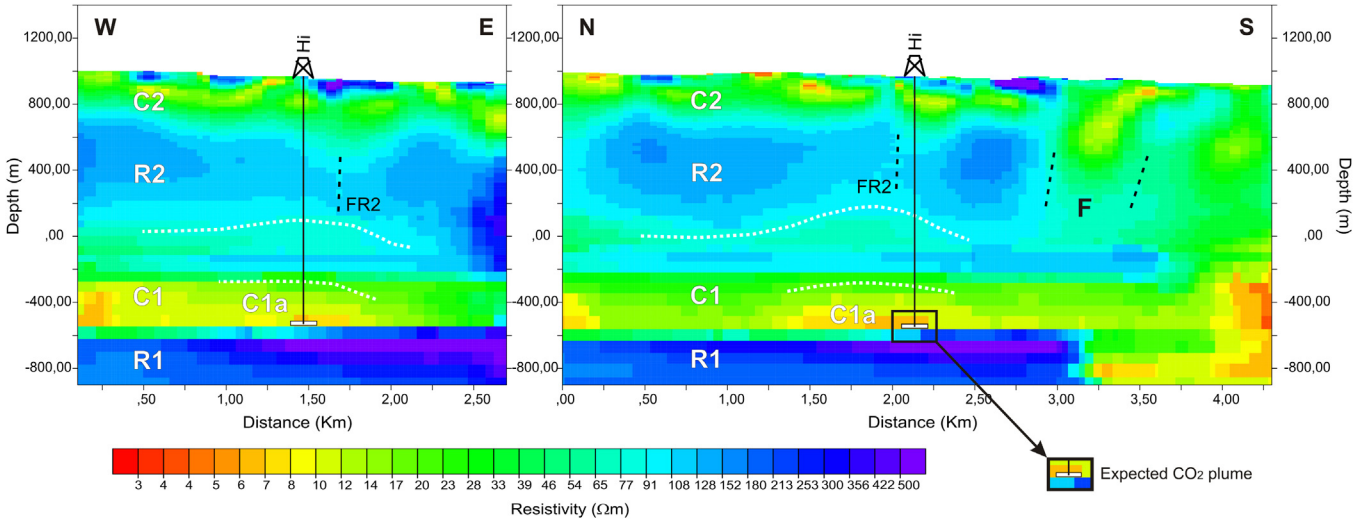

Fig. 16. NS and EW sections cutting the model by the injection well (Hi). The image shows the main resistivity layers (R1, C1, R2 and C2) and the F and FR2 fault regions. White dotted line traces the approximate soft dome-like structure of C1 and R2 layers. The expected CO_2 injection plume is indicated by a white square. Depths are given in terms of m.a.s.l.

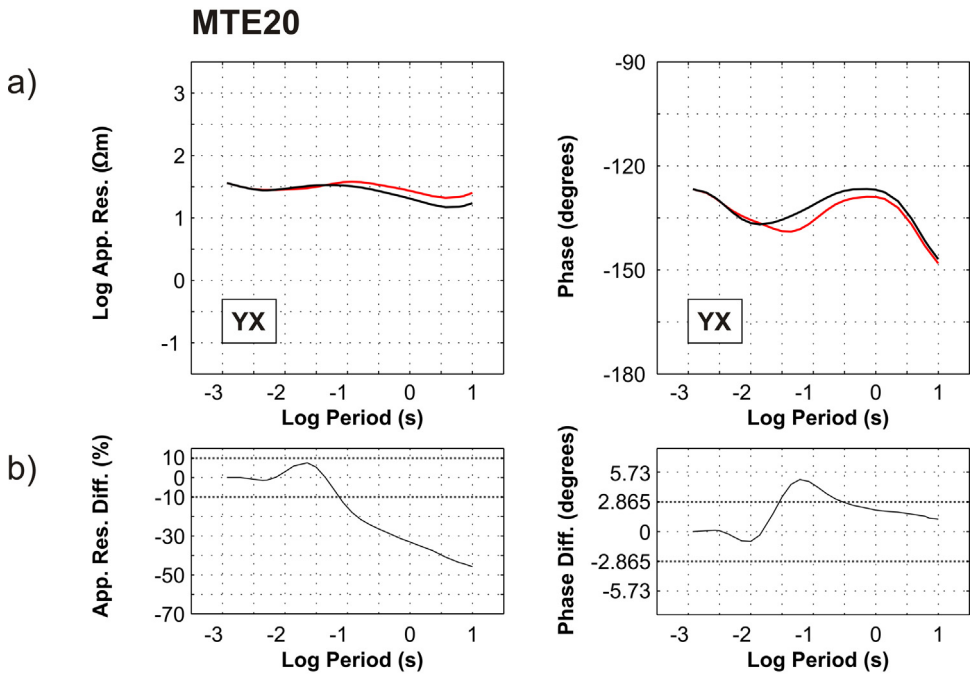

Fig. 17. Non-linear sensitivity test to study the conductive region 1 (indicated by black dotted lines in Fig. 13). (a) *YX* responses at site MTE20 of the final model (black) and the modified one (red) derived by replacing the resistivity values of the region 1 by 30 Ωm. (b) Difference between the *YX* apparent resistivity and phase responses. The differences are greater than the error floor imposed in the MT data for the inversion (10% for the *YX* apparent resistivity and 2.865 degrees for the *YX* phases). Thus the more conductive region 1 is required by sites located in the southern region of the model, mainly the ones in the MTD and MTE profiles. (For interpretation of the references to colour in this figure legend, the reader is referred to the web version of this article.)

Sets of faults

The 3D model shows the EW prolongation of the main fault F imaged in the previous 2D model (Fig. 6 in Ogaya et al., 2013). The F fault region is associated to the strike-slip movement of the Ubierna fault (Tavani et al., 2011; Quintà, 2013). The EW white dashed line in Fig. 15 indicates the approximate north-border of that region. The F fault affects all layers of the model, although it does not outcrop at surface and its top is observed at C2 layer's depth (Fig. 15a). It is characterised by a conductive behaviour, and the resistivity distribution suggests conductive fluid circulation along the fracture region. It is more conductive in the eastern part of the study

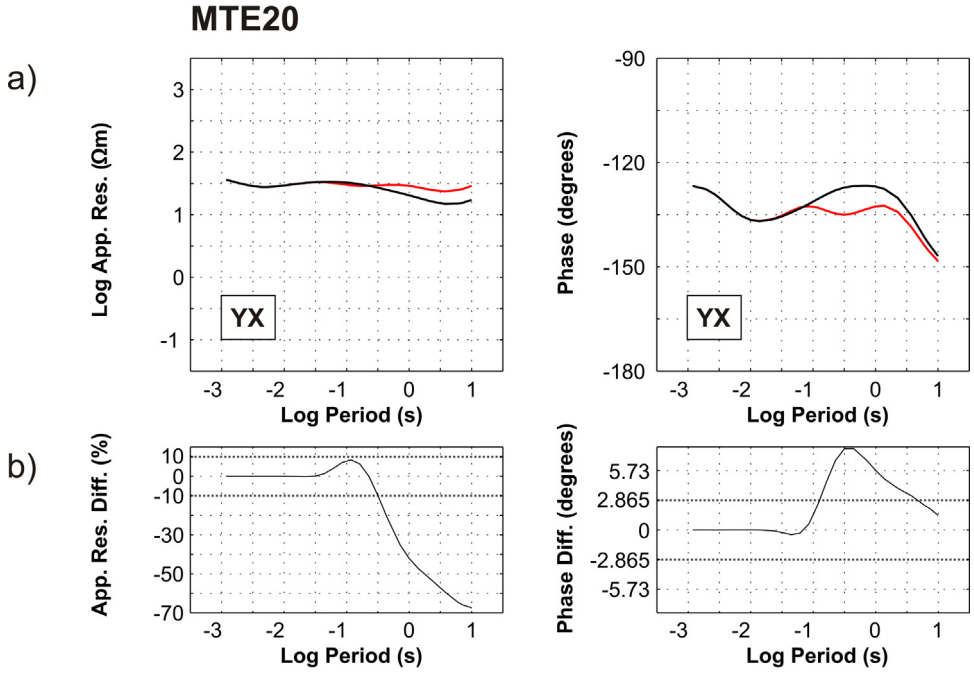

Fig. 18. Non-linear sensitivity test to study the conductive region 2 (indicated by black dotted lines in Fig. 13). (a) *YX* responses at site MTE20 of the final model (black) and the modified one (red) derived by replacing the resistivity values of the region 2 by 200 Ωm. (b) Difference between the *YX* apparent resistivity and phase responses. The differences are greater than the error floor imposed in the MT data for the inversion (10% for the *YX* apparent resistivity and 2.865 degrees for the *YX* phases). Thereby, the results indicate that there is not a continuity of the R1 layer in the southern region of the model. (For interpretation of the references to colour in this figure legend, the reader is referred to the web version of this article.)

area (Fig. 13) whereas in the western part it is less conductive and seems to be imaged as different faults (Fig. 16). These branches of the F fault are also observable in some sections of the seismic cube (Alcalde et al., 2013b). Consequently, the western part seems to be more sealed than the eastern part. Hydrogeochemical studies of surface and spring waters in the surroundings of the Hontomín URL (Buil et al., 2012; Nisi et al., 2013) found that water samples acquired in the eastern part of the F fault region could be indicative of mixing processes between deep and shallow aquifers. However, Elío et al. (2013) investigated the CO_2 flux baseline in the soil-atmosphere interface at the Hontomín site, and those authors did not find any anomaly in the F region, neither in the western nor in the eastern part.

In the eastern part of the model (under sites on the MTE profile) a more resistive behaviour of the R2 layer is observed (resistivity values up to 300 Ωm; see II and III profiles in Fig. 14). It could be due to a set of NS faults located in the east (Quintà, 2013; called EF hereafter and indicated in Fig. 14). The EF faults are located outside the modelled region, but their presence could explain the increase of the R2 layer thickness and resistivity in the eastern part of the model. The 1D resistivity model of the H3 well may differ from the others because is affected by F and EF sets of faults.

Small resistivity variations (more conductive areas) observed within the R2 layer could be associated with a set of minor faults in the Dogger and Purbeck units (Quintà, 2013). Some of these faults are indicated by FR2 in Figs. 14 and 16. In Fig. 14 are also shown the faults that cross the H wells according to well data (Quintà, 2013).

Injection area

Fig. 16 shows a NS and an EW section that cuts the 3D model by the injection well (Hi). Observed is the smooth dome-like structure of the C1 and R2 layers with Hi located close to the axis. The expected volume of CO_2 (20 kilotons, see above) is shown by a white square in Fig. 16. Since that the amount of CO_2 injection is small, none of the geoelectrical structures would appear to constitute a likely leakage pathway. However, according to the model, special attention should be paid to the possible FR2 faults neighbouring the Hi well and to the F fault (especially in the eastern part) during the monitoring of the URL.

8. Conclusions

The 3D resistivity model presented in this paper constitutes the geoelectrical baseline model of the Hontomín URL. It defines the subsurface structure in the pre-injection state and allows the detection of changes due to the CO_2 injection. It will be the reference model for the future EM monitoring experiments planned for the end of 2013.

The 3D inversion of the MT data combining different codes greatly enriched the inversion process. The 3D inversion made possible modelling the different 3D effects and improving the previous 2D model (Ogaya et al., 2013). The resistive layer located at approximately 1600 m TVD (under the conductive main reservoir-seal system) was only imaged when it was introduced into the initial model. Otherwise, the smoothness regularisation excluded exploration of that part of model space.

The final model contributes to a better understanding of the subsurface at the Hontomín site. In general, the electrical responses of each formation coincide with the ones imaged in the previous 2D model. However, the 3D model provides an important 3D spatial characterisation of the different units as well as images the prolongation of the main fault F. In this way, it is possible to determine the possible leakage pathway and design the monitoring setup according to the site requirements. Special attention needs to be paid to the possible FR2 faults neighbouring the Hi well, and to the eastern part of the F fault since the resistivity distribution there suggests conductive fluid circulation along this part of the fault.

The detailed geoelectrical characterisation presented here is an important contribution to CO_2 geological storage projects mainly for two reasons: (i) it demonstrates the valuable information that a 3D geoelectrical baseline model can provide and (ii) it shows the importance of a high-resolution reference model to define the monitoring requirements. Three-dimensional magnetotelluric surveys are complementary to other 3D reflection seismic and gravimetric characterisation studies, and, due to electrical conductivity's sensitivity to fluid flow, makes for a method with superior resolution of particular aspects of interest and importance for CO_2 storage and long-term monitoring.

Acknowledgements

This project has been partly financed by funds coming from the Spanish Ministry of Industry, Tourism and Trade, through the CIUDEN-UB Geomodels agreement related to the Development and Adaptation of Electromagnetic techniques: Characterisation of Storage Sites. This project is co-financed by the European Union through the Technological Development Plant of Compostilla OXYCFB300 Project (European Energy Programme for Recovery). This work was also developed in the framework of the Spanish MCI project PIER-CO_2 (CGL2009-07604). It is a contribution of the Research Group of Geodynamics and Basin Analysis (2009SGR1198) of the Generalitat de Catalunya and the Research Institute GEOMODELS. Xènia Ogaya was supported by the Fundación Ciudad de la Energía (CIUDEN) research training programme and by the Universitat de Barcelona (UB) through the Ajut per a Personal Investigador en Formació (APIF). EXES-UB group is thanked for their help in the MT data acquisition. The authors also want to thank Gary Egbert and Anna Kelbert for providing the ModEM code; Weerachai Siripunvaraporn for providing WSINV3DMT code; the Irish Centre for High-End Computing (ICHEC) for availing the Stokes cluster to carry out the numerical computations and Jan Vozar for his advice on the 3D inversion process. The authors sincerely thank the Associate Editor Charles Jenkins and the anonymous reviewers for their useful comments on the manuscript. Last, but not least, Modesto Montoto and Andrés Pérez-Estaún are thanked for their continuous support.

References

Alcalde, J., Martí, D., Calahorrano, A., Marzán, I., Ayarza, P., Carbonell, R., Juhlin, C., Pérez-Estaún, A., 2013a. Active seismic characterization experiments of the Hontomín research facility for geological storage of CO_2, Spain. Int. J. Greenhouse Gas Control 19, 785–795, http://dx.doi.org/10.1016/j.ijggc.2013.01.039.

Alcalde, J., Martí, D., Juhlin, C., Malehmir, A., Sopher, D., Saura, E., Marzán, I., Ayarza, P., Calahorrano, A., Pérez-Estaún, A., Carbonell, R., 2013b. 3-D reflection seismic imaging of the Hontomín structure in the Basque-Cantabrian basin (Spain). Solid Earth 4, 481–496, http://dx.doi.org/10.5194/se-4-481-2013.

Alemu, B.L., Aker, E., Soldal, M., Johnsen, Ø., Aagaard, P., 2011. Influence of CO_2 on rock physics properties in typical reservoir rock: a CO_2 flooding experiment of brine saturated sandstone in a CT-scanner. Energy Proc. 4, 4379–4386, http://dx.doi.org/10.1016/j.egypro.2011.02.390.

Archie, G.E., 1942. The electrical resistivity log as an aid in determining some reservoir characteristics. Trans. AIME 146, 54–67.

Avdeev, D.B., 2005. Three-dimensional electromagnetic modelling and inversion from theory to application. Surveys Geophys. 26 (6), 767–799, http://dx.doi.org/10.1007/s10712-005-1836-2.

Bedrosian, P.A., 2007. MT+, integrating magnetotellurics to determine earth structure, physical state, and processes. Surveys Geophys. 28, 121–167, http://dx.doi.org/10.1007/s10712-007-9019-6.

Benjumea, B., Macau, A., Figueres, S., Gabàs, S., Sendra, R., Marzán, I., 2012. Testificación geofísica de los sondeos de investigación hidrogeológica de Hontomín (Burgos). IGC – Institut Geològic de Catalunya Technical Report, GA-002/12. Generalitat de Catalunya, pp. 36.

Bergmann, P., Schmidt-Hattenberger, C., Kiessling, D., Rücker, C., Labitzke, T., Henninges, J., Baumann, G., Schütt, H., 2012. Surface-downhole electrical resistivity

tomography applied to monitoring of CO_2 storage at Ketzin, Germany. Geophysics 77, B253–B267, http://dx.doi.org/10.1190/geo2011-0515.1.
Börner, R.U., 2010. Numerical modelling in geo-electromagnetics: advances and challenges. Surv. Geophys. 31 (2), 225–245, http://dx.doi.org/10.1007/s10712-009-9087-x.
Börner, J.H., Herdengen, V., Repke, J.U., Spitzer, K., 2013. The impact of CO_2 on the electrical properties of water bearing porous madia-laboratory experiments with respect to carbon capture and storage. Geophys. Prospect. 61 (Suppl. 1), 446–460, http://dx.doi.org/10.1111/j.1365-2478.2012.01129.x.
Bourgeois, B., Girard, J.F., 2010. First modelling results of the EM response of a CO_2 storage in the Paris basin. Oil Gas Sci. Technol. Rev. – IFP 65 (4), 597–614, http://dx.doi.org/10.2516/ogst/2009076.
Buil, B., Gómez, P., Peña, J., Garralón, A., Galarza, C., Durán, J.M., Domínguez, R., Escribano, A., Turrero, M.J., Robredo, L.M., Sánchez, L., 2012. Caracterización y monitorización hidrogeoquímica de los acuíferos superiores a la formación almacenamiento de CO2 (Hontomín, Burgos) y actualización de la caracterización de aguas superficiales. Technical report CIEMAT/DMA/2G010/1/2012.
Caldwell, T.G., Bibby, H.M., Brown, C., 2004. The magnetotelluric phase tensor. Geophys. J. Int. 158, 457–469, http://dx.doi.org/10.1111/j.1365-246X.2004.02281.x.
Canal, J., Delgado, J., Falcón, I., Yang, Q., Juncosa, R., Barrientos, V., 2013. Injection of CO_2-saturated water through a siliceous sandstone plug from the Hontomin Test Site (Spain): experiments and modeling. Environ. Sci. Technol. 47 (1), 159–167, http://dx.doi.org/10.1021/es3012222.
Chave, A.D., Jones, A.G., 2012. The Magnetotelluric Method: Theory and Practice. Cambridge University Press, Cambridge (UK), ISBN 978-0-521-81927-5.
Chave, A.D., Thomson, D.J., 2004. Bounded influence magnetotelluric response function estimation. Geophys. J. Int. 157, 988–1006, http://dx.doi.org/10.1111/j.1365-246X. 2004.02203.x.
Egbert, G.D., Booker, J.R., 1986. Robust estimation of Geomagnetic transfer functions. Geophys. J. R. Astronom. Soc. 87, 173–194.
Egbert, G.D., Kelbert, A., 2012. Computational recipes for EM inverse problems. Geophys. J. Int. 189 (1), 251–267, http://dx.doi.org/10.1111/j.1365-246X.2011.05347.x.
Elío, J., Nisi, B., Ortega, M.F., Mazadiego, L.F., Vaselli, O., Grandia, F., 2013. CO_2 soil flux baseline at the technological development plant for CO_2 injection at Hontomin (Burgos, Spain). Int. J. Greenhouse Gas Control 18, 224–236, http://dx.doi.org/10.1016/j.ijggc.2013.07.013.
Escalas, M., Queralt, P., Ledo, J., Marcuello, A., 2013. Polarisation analysis of magnetotelluric time series using a wavelet-based scheme: a method for detection and characterisation of cultural noise sources. Phys. Earth Planet. Inter. 218, 31–50, http://dx.doi.org/10.1016/j.pepi.2013.02.006.
Farquharson, C.G., Craven, J.A., 2009. Three-dimensional inversion of magnetotelluric data for mineral exploration: an example from the McArthur River uranium deposit, Saskatchewan, Canada. J. Appl. Geophys. 68 (4), 450–458, http://dx.doi.org/10.1016/j.jappgeo.2008.02.002.
Gamble, T.D., Goubau, W.M., Clarke, J., 1979. Magnetotellurics with a remote magnetic reference. Geophysics 44, 53–68.
Giese, R., Henninges, J., Lüth, S., Morozova, D., Schmidt-Hattenberger, C., Würdemann, H., Zimmer, M., Cosma, C., Juhlin, C., CO2SINK Group, 2009. Monitoring at the CO_2SINK site: a concept integrating geophysics. Geochem. Microbiol. Energy Proc. 1, 2251–2259, http://dx.doi.org/10.1016/j.egypro.2009.01.293.
Ghaedrahmati, R., Moradzadeh, A., Fathianpour, N., Lee, S.K., Porkhial, S., 2013. 3-D inversion of MT data from the Sabalan geothermal field, Ardabil, Iran. J. Appl. Geophys. 93, 12–24, http://dx.doi.org/10.1016/j.jappgeo.2013.03.006.
Girard, J.F., Coppo, N., Rohmer, J., Bourgeois, B., Naudet, V., Schmidt-Hattenberger, C., 2011. Time-lapse CSEM monitoring at Ketzin (Germany) CO_2 injection using 2xMAM configuration. Energy Proc. 4, 3322–3329.
Groom, R.W., Bailey, R.C., 1989. Decomposition of magnetotelluric impedance tensor in the presence of local three-dimensional galvanic distortion. J. Geophys. Res. 94, 1913–1925.
He, Z., Hu, Z., Luo, W., Wang, C., 2010. Mapping reservoirs based on resistivity and induced polarization derived from continuous 3D magnetotelluric profiling: case study from Qaidim basin, China. Geophysics 75 (1), B25–B33, http://dx.doi.org/10.1190/1.3279125.
Heise, W., Caldwell, T.G., Bibby, H.M., Bannister, S.C., 2008. Three-dimensional modeling of the magnetotelluric data from the Rotakawa geothermal field, Taupo Volcanic Zone, New Zeland. Geophys. J. Int. 173, 740–750, http://dx.doi.org/10.1111/j.1365-246X.2008.03737.x.
Hoversten, G.M., Gasperikova, E., 2005. Non-seismic geophysical approaches to monitoring. In: Thomas, D.C., Benson, S.M. (Eds.), Carbon Dioxide Capture for Storage in Deep Geologic Formations, vol. 2. Elsevier Ltd., Oxford, UK, pp. 1071–1112.
Ingham, M.R., Bibby, H.M., Heise, W., Jones, K.A., Cairns, P., Dravitzki, S., Bennie, S.L., Caldwell, T.G., Ogawa, Y., 2009. A magnetotelluric study of Mount Ruapehu volcano, New Zealand. Geophys. J. Int. 179 (2), 887–904, http://dx.doi.org/10.1111/j.1365-246X.2009.04317.x.
IPCC – Intergovernmental Panel on Climate Change, 2005. In: Metz, B., Davidson, O., de Coninck, H.C., Loos, M., Meyer, L.A. (Eds.), IPCC Special Report on Carbon Dioxide Capture and Storage. Prepared by Wozzrking Group III of the Intergovernmental Panel on Climate Change. Cambridge University Press, Cambridge, United Kingdom and New York, NY, USA.
JafarGandomi, A., Curtis, A., 2011. Detectability of petrophysical properties of subsurface CO_2-saturated aquifer reservoirs using surface geophysical methods. Lead. Edge 30 (10), 1112–1121.
Jones, A.G., 2012. Distortion of magnetotelluric data: its identification and removal. In: Chave, A.D., Jones, A.G. (Eds.), The Magnetotelluric Method: Theory and Practice. Cambridge University Press, Cambridge (UK), ISBN 978-0-521-81927-5.
Kiessling, D., Schmidt-Hattenberger, C., Schuett, H., Schilling, F., Krueger, K., Schoebel, B., Danckwardt, E., Kummerow, J., CO2SINK Group, 2010. Geoelectrical methods for monitoring geological CO_2 storage: first results from cross-hole and surface-downhole measurements from the CO2SINK test site at Ketzin (Germany). Int. J. Greenhouse Gas Control 4 (5), 816–826, http://dx.doi.org/10.1016/j.ijggc.2010.05.001.
Kiyan, D., Jones, A.G., Vozar, J., 2014. The inability of magnetotelluric off-diagonal impedance tensor elements to sense oblique conductors in 3-D inversion. Geophys. J. Int. 196, 1351–1364, http://dx.doi.org/10.1093/gji/ggt470.
Ledo, J., Jones, A.G., 2005. Upper mantle temperature determined from combining mineral composition, electrical conductivity laboratory studies and magnetotelluric field observations: application to the intermontane belt, Northern Canadian Cordillera. Earth Sci. Lett. 236, 258–268, http://dx.doi.org/10.1016/j.epsl.2005.01.044.
Ledo, J., Queralt, P., Martí, A., Jones, A.G., 2002. Two-dimensional interpretation of three-dimensional magnetotelluric data: an example of limitations and resolution. Geophys. J. Int. 150 (1), 127–139, http://dx.doi.org/10.1046/j.1365-246X.2002.01705.x.
Lumley, D., 2010. 4D seismic monitoring of CO2 sequestrattion. Lead. Edge 29 (2), 150–155, http://dx.doi.org/10.1190/1.3304817.
MacGregor, L., 2012. Integrating seismic, CSEM, and well log data for reservoir characterization. Lead. Edge 31 (3), 268–277.
Mackie, R.L., Madden, T.R., 1993. Three dimensional magnetotelluric inversion using conjugate gradients. Geophys. J. Int. 115, 215–229, http://dx.doi.org/10.1111/j.1365-246X.1993.tb05600.x.
Márquez, M., Jurado, M.J., 2011. Petrophysical characterization of a CO_2 storage reservoir using well logs. Geophys. Res. Abstr. 13, EGU2011-6891-3. EGU General Assembly 2011.
Martí, A., Queralt, P., Ledo, J., 2009. WALDIM: A code for the dimensionality analysis of magnetotelluric data using rotational invariants of the magnetotelluric tensor. Comput. Geosci. 35 (12), 2295–2303, http://dx.doi.org/10.1016/j.cageo.2009.03.004.
Miensopust, M.P., Queralt, P., Jones, A.G., the 3D MT modellers, 2013. Magnetotelluric 3D inversion – a recapitulation of two successful workshops on forward and inversion code testing and comparison. Geophys. J. Int. 193 (3), 1216–1238, http://dx.doi.org/10.1093/gji/ggt066.
Muñoz, J.A., 2002. The Pyrenees. In: Gibbons, W., Moreno, T. (Eds.), The Geology of Spain. Geological Society, London, pp. 370–385.
Nakatsuka, Y., Xue, Z., Garcia, H., Matsuoka, T., 2010. Experimental study on CO_2 monitoring and quantification of stored CO_2 in saline formations using resistivity measurements. Int. J. Greenhouse Gas Control 4, 209–216, http://dx.doi.org/10.1016/j.ijggc.2010.01.001.
NETL-National Energy Technology Laboratory, U.S. Department of Energy, 2009. Monitoring, Verification, and Accounting of CO2 Stored in Deep Geologic Formations. DOE Document: DOE/NETL-311/081508, Accessed October, 2013. http://www.netl.doe.gov/technologies/carbon_seq/refshelf/MVA_Document.pdf
Newman, G.A., Gasperikova, E., Hoversten, G.M., Wannamaker, P.E., 2008. Three-dimensional magnetotelluric characterization of the Coso geothermal field. Geothermics 37, 369–399, http://dx.doi.org/10.1016/j.geothermics.2008.02.006.
Newman, G.A., Recher, S., Tezkan, B., Neubauer, M., 2003. 3D inversion of a scalar radio magnetotelluric field data set. Geophysics 68 (3), 791–802, http://dx.doi.org/10.1190/1.1581032.
Nisi, B., Vaselli, O., Tassi, F., Elío, J., Delgado Huertas, A., Mazadiego, L.P., Ortega, M.F., 2013. Hydrogeochemistry of surface and spring waters in the surroundings of the CO_2 injection site at Hontomín-Huermeces (Burgos Spain). Int. J. Greenhouse Gas Control 14, 151–168, http://dx.doi.org/10.1016/j.ijggc.2013.01.012.
Ogaya, X., Ledo, J., Queralt, P., Marcuello, A., Quintà, A., 2013. First geoelectrical image of the subsurface of the Hontomín site (Spain) for CO_2 geological storage: a magnetotelluric 2D characterization. Int. J. Greenhouse Gas Control 13, 168–179, http://dx.doi.org/10.1016/j.ijggc.2012.12.023.
Ogaya, X., Queralt, P., Ledo, J., Marcuello, A., Jones, A.G., 2012. Preliminary results of the 3-D magnetotelluric characterization of the subsurface of the Technology Demonstration Plant of Hontomín (Burgos, Spain) for geological storage of CO_2. In: Zurutuza, J. (Ed.), 7AHPGG: Proceedings. Portuguese-Spanish Assembly of Geodesy and Geophysics. , ISBN 978-84-941323-1-5, pp. 703–708.
Parker, R.L., 1980. The inverse problem of electromagnetic induction: existence and construction of solutions based on incomplete data. J. Geophys. Res. 85 (B8), 4421–4428, http://dx.doi.org/10.1029/JB085iB08p04421.
Parker, R.L., Whaler, K.A., 1981. Numerical methods for establishing solutions to the inverse problem of electromagnetic induction. J. Geophys. Res. 86 (B10), 9574–9584, http://dx.doi.org/10.1029/JB086iB10p09574.
Piña-Varas, P., Ledo, J., Queralt, P., Roca, E., García-Lobón, J.L., Ibarra, P., Biete, C., 2013. Two-dimensional magnetotelluric characterization of the El Hito Anticline (Loranca Basin, Spain). J. Appl. Geophys. 95, 121–134, http://dx.doi.org/10.1016/j.jappgeo.2013.06.002.
Quintà, A., (Ph.D. Thesis) 2013. El patrón de fracturación alpina en el sector suroccidental de los Pirineos Vascos. Universitat de Barcelona, Barcelona, Spain, pp. 153.
Rosell, O., Martí, A., Marcuello, A., Ledo, J., Queralt, P., Campanyà, J., 2011. Deep electrical resistivity structure of the northern Gibraltar Arc (western mediterranean): evidence of lithospheric slab break-off. Terra Nova 23 (3), 179–186, http://dx.doi.org/10.1111/j.1365-3121.2011.00996.x.

Rubio, F.M., Ayala, C., Gumiel, J.C., Rey, C., 2011. Caracterización mediante campo potencial y teledetección de la estructura geológica seleccionada para planta de desarrollo tecnológico de almacenamiento geológico de CO2 en Hontomín (Burgos). IGME-Instituto Geológico y Minero de España Technical Report, pp. 182.

Sato, K., Mito, S., Horie, T., Ohkuma, H., Saito, H., Watanabe, J., Yoshimura, T., 2011. Monitoring and simulation studies for assessing macro- and meso-scale migration of CO_2 sequestered in an onshore aquifer: experiences from the Nagaoka pilot site, Japan. Int. J. Greenhouse Gas Control 5, 125–137, http://dx.doi.org/10.1016/j.ijggc.2010.03.003.

Siripunvaraporn, W., 2012. Three-dimensional magnetotelluric inversion: an introductory guide for developers and users. Surv. Geophys. 33 (1), 5–27, http://dx.doi.org/10.1007/s10712-011-9122-6.

Siripunvaraporn, W., Egbert, G., Lenbury, Y., Uyeshima, M., 2005. Three-dimensional magnetotelluric inversion: data-space method. Phys. Earth Planet. Inter. 150, 3–14, http://dx.doi.org/10.1016/j.pepi.2004.08.023.

Streich, R., Becken, M., Ritter, O., 2010. Imaging of CO_2 storage sites, geothermal reservoirs, and gas shales using controlled-source magnetotellurics: modeling studies. Chem. Erde-Geochem. 70 (3), 63–75, http://dx.doi.org/10.1016/j.chemer.2010.05.004.

Tavani, S., Quintà, A., Granado, P., 2011. Cenozoic right-lateral wrench tectonics in the Western Pyrenees (Spain): the Ubierna Fault System. Tectonophysics 509, 238–253, http://dx.doi.org/10.1016/j.tecto.2011.06.013.

Tuncer, V., Unsworth, M.J., Siripunvaraporn, W., Craven, J.A., 2006. Exploration for unconformity-type uranium deposits with audiomagnetotellurics data: a case study from the McArthur River mine, Saskatchewan, Canada. Geophysics 71 (6), B201–B209, http://dx.doi.org/10.1190/1.2348780.

Ugalde, A., Villaseñor, A., Gaite, B., Casquero, S., Martí, D., Calahorrano, A., Marzán, I., Carbonell, R., Estaún, A.P., 2013. Passive seismic monitoring of an experimental CO_2 geological storage site in Hontomín (Northern Spain). Seismol. Res. Lett. 84 (1), 75–84, http://dx.doi.org/10.1785/0220110137.

Vilamajó, E., Queralt, P., Ledo, J., Marcuello, A., 2013. Feasibility of monitoring the Hontomín (Burgos Spain) CO_2 storage site using deep EM source. Surv. Geophys. 34, 441–461, http://dx.doi.org/10.1007/s10712-013-9238-y.

Weaver, J.T., Agarwal, A.K., Lilley, F.E.M., 2000. Characterisation of the magnetotelluric tensor in terms of its invariants. Geophys. J. Int. 141 (2), 321–336, http://dx.doi.org/10.1046/j.1365-246X.2000.00089.x.

Xiao, Q., Cai, X., Xu, X., Liang, G., Zhang, B., 2010. Application of the 3D magnetotelluric inversion code in a geologically complex area. Geophys. Prospect. 58 (6), 1177–1192, http://dx.doi.org/10.1111/j.1365-2478.2010.00896.x.

Zhdanov, M.S., Wan, L., Gribenko, A., Čuma, M., Key, K., Constable, S., 2011. Large-scale 3D inversion of marine magnetotelluric data: Case study from the Gemini prospect, Gulf of Mexico. Geophysics 76 (1), F77–F87, http://dx.doi.org/10.1190/1.3526299.